Accurate radiation boundary conditions for the two-dimensional wave equation on unbounded domains ☆

Lonny L. Thompson *, Runnong Huan, Dantong He

Department of Mechanical Engineering, Clemson University, 102 Fluor Daniel Engr. Innov. Bldg., Clemson, SC 29634-0921, USA

Abstract

A recursive sequence of radiation boundary conditions first given by Hagstrom and Hariharan [Appl. Numer. Math. 27 (1998) 403] for the time-dependent wave equation in a two-dimensional exterior region are re-derived based on direct application of the hierarchy of local boundary operators of Bayliss and Turkel [Commun. Pure Appl. Math. 33 (1980) 707] and a recursion relation for the expansion coefficients appearing in an asymptotic wave expansion. By introducing a decomposition into tangential Fourier modes on a circle we reformulate the sequence of local boundary conditions in integro-differential form involving systems of first-order temporal equations for auxiliary functions associated with each mode and the Fourier transform of the solution evaluated on the boundary. The auxiliary functions are recognized as residuals of the local boundary operators acting on the asymptotic wave expansion. Direct finite element implementations for the original local sequence of boundary conditions are compared to implementations of the Fourier transformed auxiliary functions. We show that both implementations easily fit into a standard finite element discretization provided that independent time integration algorithms are used for the interior and boundary equations with coupling through the boundary force vectors at each time step. For both of our direct and modal finite element implementations, the amount of work and storage is less than that required for the finite element calculation in the interior region within the boundary. One advantage of the tangential modal implementation is that far-field solutions may be computed separately for each Fourier mode without saving lengthy time-history data at interior points. Numerical studies confirm the progressive improvement in accuracy with increasing number of auxiliary functions included. © 2001 Elsevier Science B.V. All rights reserved.

Keywords: Radiation boundary conditions; Wave equation; Finite element method; Scattering; Unbounded domains

1. Introduction

When simulating sound wave radiation or scattering form vibrating structures submerged in an acoustic medium which extends to infinity, with domain based computational methods, the far-field is truncated at a finite boundary. The impedance of the far-field may then be represented on this truncation boundary by various methods including, exact and approximate radiation boundary conditions (RBCs), infinite elements, and absorbing sponge layers. Ideally, the truncation boundary would be placed as close as possible to the source, and the radiation boundary treatment would be capable of arbitrary accuracy at a cost and memory not exceeding that of the interior solver. A survey article on many of the various boundary treatments available is given in [3]. In [4], a review of the theory for several of the most promising methods for time-dependent wave propagation is given. Finite element discretization of the bounded computational region allows for a natural coupling of an acoustic fluid region to an elastic radiator/scatterer in applications

---

* Corresponding author.
  E-mail address: lonny.thompson@ces.clemson.edu (L.L. Thompson).

of structural acoustics [5–7]. The accurate numerical modeling of wave propagation is also important in many other fields of physics including computational electromagnetics and aeroacoustics.

If accurate boundary treatments are used, the finite computational region may be reduced so that the truncation boundary is relatively close to the radiator, and fewer grids than otherwise would be possible may be used, resulting in considerable savings in both cpu time and memory. In the frequency domain, several accurate and efficient methods for representing the impedance of the far-field are well understood, including the Dirichlet-to-Neumann (DtN) map [8–11], and infinite elements [12]. However, efficient evaluation of accurate boundary treatments for the time-dependent wave equation on unbounded spatial domains has long been an obstacle for the development of reliable solvers for time domain simulations, primarily because of the large non-local time-history required of exact conditions on arbitrary boundaries.

To avoid the time-history implied by exact conditions such as the Kirchoff boundary integral method, a standard approach used by early researchers was to apply local (differential) boundary operators which annihilate leading terms in the radial multipole expansion for outgoing wave solutions. A well known hierarchy of boundary conditions developed for circular and spherical truncation boundaries are the local operators derived by Bayliss and Turkel [13]. In theory, these operators allow for increasing orders of accuracy. However, as the order of these local RBCs increases they become increasingly difficult to implement in standard numerical methods due to the occurrence of high-order derivatives on the artificial boundary. For this reason, they have been limited to simple first- and second-order conditions, which for many problems of practical interest give inaccurate solutions.

In recent years, new boundary treatments have been developed which dramatically improve both the accuracy and efficiency of time domain simulations compared to simple approximate RBCs. One promising approach is the application of the 'perfectly matched layer' (PML) technique [14,15] which introduces an external layer designed to absorb outgoing waves. A difficulty with the PML technique is that the errors scale with the time length of the simulation, and thus may be unacceptable for large time intervals [4]. Another treatment of the unbounded domain is the use of local wave-envelope (infinite) elements based on conjugated weight functions [16–18]. A difficulty with wave-envelope elements is that they introduce local non-symmetric matrices which destroy the symmetric structure of the semi-discretization of the interior domain. In the frequency domain, at high radial-orders the global matrices exhibit poor conditioning and may become unstable [12]. This behavior has not been demonstrated for the time-dependent counterpart, however, it is noted that the transient infinite elements have only been implemented for low radial orders, typically up to order 3 [16–19].

In [20,21], exact local non-reflecting boundary conditions (NRBC) were derived for the three-dimensional wave equation on a sphere. In [22], this NRBC was rederived based on direct application of a result given in [23], with improved scaling of the first-order system of equations associated with the NRBC. Formulation of the NRBC in standard semi-discrete finite element methods with several alternative implicit and explicit time-integrators is reported in [22]. In [24], a method is described for efficient calculation of far field solutions. In [25], a modified version of the exact NRBC first derived in [21], is implemented in a finite element formulation. The modified version may be viewed as an extension of the second-order local boundary operator derived by Bayliss and Turkel [13], and gives improved accuracy when only a few harmonics are included in the spherical expansion/transform. Extensions to the semi-infinite problem resulting from radiating structures mounted in a half-plane are given in [26]. In [26] explicit time-integrators are used to solve the semi-discrete finite element equations in the interior domain concurrently with implicit solvers for the auxiliary variables in the modified boundary condition formulated in [25].

In [1,27], the recursive sequence of asymptotic and exact local RBCs for the three-dimensional wave equation, first derived by Hagstrom and Hariharan [28], are reformulated using a harmonic expansion on a sphere. By introducing a decomposition into spherical harmonics the sequence of local boundary conditions is reformulated as a problem involving systems of first-order temporal equations, similar to that used in [20,22]. With this reformulation, the auxiliary functions are recognized as residuals of the local boundary operators acting on the radial wave expansion. With the number of time-dependent auxiliary variables in the ordinary differential equation for each harmonic equal to the mode number, the RBCs are exact. If fewer equations are used, then the boundary conditions from high-order accurate asymptotic approximations to the exact condition, with corresponding reduction in work and memory. The harmonic for-

mulation of the RBCs given [27] has several advantages over the NRBC derived in [20,22] including a banded tri-diagonal coefficient matrix for the auxiliary variables, reduced memory and computational work needed to store and solve the auxiliary functions for each harmonic, and the ability to vary separately the radial truncation and transverse modal orders of the RBC.

In this paper we extend the ideas used in [27] to reformulate the sequence of high-order local boundary conditions given in [28] in terms of a Fourier mode expansion for the two-dimensional wave equation on a circular boundary. We rederive this sequence based on direct application of the hierarchy of local boundary operators of Bayliss and Turkel [13] and a recursion relation for the expansion coefficients appearing in the 2D asymptotic wave expansion. These boundary conditions are local and involve auxiliary variables to remove the high order derivatives in radial r and time t dimensions, present in the original boundary operators of Bayliss and Turkel. With this reformulation, the auxiliary functions are recognized as residuals of the local boundary operators acting on the asymptotic wave expansion.

Outside the circular artificial boundary we replace the solution by a Fourier series expansion with $N_T = 2N + 1$ terms in the tangential variable. For each mode the asymptotic expansion in r is truncated after P terms. This leads to a system of ordinary differential equations at most of dimension P for each Fourier mode and enables the update in time of the (Fourier transformed) auxiliary variables. This reformulation effectively recasts the two-dimensional boundary conditions in [28] to a formulation given in [27] for the three-dimensional wave equation on a sphere. It easily fits into a standard finite element discretization, which is used in the interior region. For scattering problems, a finite element formulation for the total field, which avoids explicitly computing normal derivatives on a geometrically complex scattered surface is presented. With this formulation, the variational equation is modified by including the incident wave field on the circular radiation boundary. On a circle, the normal derivative simplifies to a radial derivative which can easily be computed a priori. To compute the far-field solution we use a second-order finite difference discretization of the radial wave equation separately for each Fourier mode, similar to that used in [24]. Using trig recursion of Fast Fourier Transform (FFT) methods, we show that the work per time step and storage associated with calculation of the auxiliary functions and the inner-products required for the Fourier transforms is less than the work and storage required for the finite element calculation in the interior domain.

Direct finite element implementations for the original local sequence of boundary conditions are compared to implementations of the Fourier transformed auxiliary functions. We show that the direct implementation of the auxiliary functions preserves the symmetry of the semi-discrete finite element equations in the interior region provided that independent time integration algorithms are used for the interior and boundary equations with coupling through the boundary force vectors at each time step. For both of our direct and modal finite element implementations, we show that the amount of work and storage is less than that required for the finite element calculation in the interior region within the boundary.

Numerical studies are performed for radiation and scattering from circular and elliptic cylinders with comparisons to analytic solutions. The results are used to assess the accuracy of the RBCs as a function of the number of terms N included in the Fourier expansion, the number of auxiliary variables P included, the radial distance R, and the frequency ω. Comparisons are made between the direct and Fourier expansion methods with particular attention given to the stability of various time-integration algorithms for solution of the coupled interior and boundary equations.

2. Two-dimensional wave equation of unbounded domains

We consider time-dependent waves in an infinite two-dimensional region $\mathscr{R} \subset \mathbb{R}^2$, surrounding on object with surface $\mathscr{S}$. For computation, the unbounded region $\mathscr{R}$ is truncated by an artificial circular boundary Γ, or radius $\|\boldsymbol{x}\| = R$. We then denote by $\Omega \subset \mathscr{R}$, the finite subdomain bounded by $\partial\Omega = \Gamma \cup \mathscr{S}$, see Fig. 1. Within Ω, the solution $\phi(\boldsymbol{x}, t) : \Omega \times \mathbb{R}^+ \mapsto \mathbb{R}$, satisfies the scalar wave equation

$$\frac{1}{c^2} \frac{\partial^2 \phi}{\partial t^2} = \nabla^2 \phi + f(\boldsymbol{x}, t), \quad \boldsymbol{x} \in \Omega, \ t \in \mathbb{R}^+ \tag{1}$$
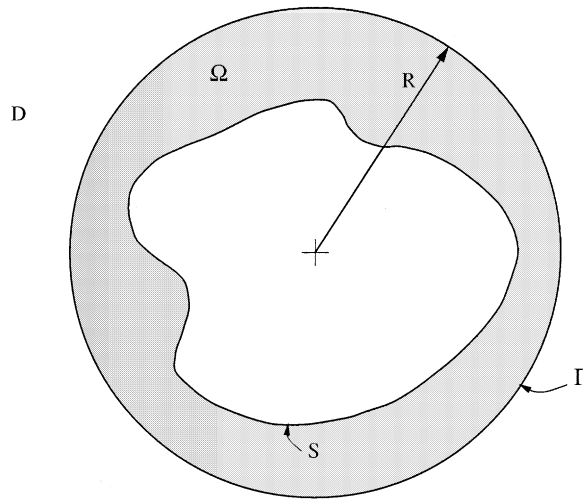
Fig. 1. Illustration of two-dimensional unbounded region $\mathscr{R}$ surrounding a scatterer $\mathscr{S}$. The computational domain $\Omega \subset \mathscr{R}$ is surrounded by a circular truncation boundary Γ of radius R, with exterior region $\mathscr{D} = \mathscr{R} - \Omega$.

with initial conditions

$$\phi(\boldsymbol{x}, 0) = \phi_0(\boldsymbol{x}), \quad \frac{\partial \phi}{\partial t}(\boldsymbol{x}, 0) = \dot{\phi}_0(\boldsymbol{x}), \quad \boldsymbol{x} \in \Omega \tag{2}$$

and driven by the time-dependent boundary condition on the surface $\mathscr{S}$:

$$\alpha \frac{\partial \phi}{\partial n} + \beta \frac{\partial \phi}{\partial t} + \gamma \phi = g(\boldsymbol{x}, t), \quad \boldsymbol{x} \in \mathscr{S}, \ t \in \mathbb{R}^+. \tag{3}$$

The wave speed c, and α, β, γ are real, and we assume $c > 0$, and $\alpha, \beta \geqslant 0$. The source f and initial data ϕ_0 and $\dot{\phi}_0$ are assumed to be confined to the computational domain Ω, so that in the exterior region $\mathscr{D} = \mathscr{R} - \Omega$, i.e., the infinite region outside Γ, the scalar field $\phi(\boldsymbol{x}, t)$ satisfies the homogeneous form of the wave equation

$$\frac{1}{c^2} \frac{\partial^2 \phi}{\partial t^2} = \nabla^2 \phi, \quad \boldsymbol{x} \in \mathscr{D}, \ t \in \mathbb{R}^+, \tag{4}$$

$$\phi(\boldsymbol{x}, 0) = 0, \quad \frac{\partial \phi}{\partial t}(\boldsymbol{x}, 0) = 0, \quad \boldsymbol{x} \in \Omega. \tag{5}$$

3. Non-reflecting boundary kernels

In polar coordinates (r, θ), the external region is defined as, $\mathscr{D} = \{r \geqslant R, \ 0 \leqslant \theta < 2\pi\}$, and the wave equation takes the form

$$\frac{1}{c^2} \frac{\partial^2 \phi}{\partial t^2} = \frac{\partial^2 \phi}{\partial r^2} + \frac{1}{r} \frac{\partial \phi}{\partial r} + \frac{1}{r^2} \frac{\partial^2 \phi}{\partial \theta^2}. \tag{6}$$

The general solution to (6) is given by the Fourier expansion

$$\phi(r, \theta, t) = \sum_{n=-\infty}^{\infty} \phi_n(r, t) \mathrm{e}^{\mathrm{i} n \theta} \tag{7}$$

with complex-valued Fourier modes $\phi_n(r, t) : [R, \infty] \times \mathbb{R}^+ \mapsto \mathbb{C}$, defined by the tangential Fourier transform:

$$\phi_n(r,t) = \frac{1}{2\pi} \int_0^{2\pi} \phi(r,\theta,t) e^{-in\theta} \, d\theta. \tag{8}$$

Here $\phi_n = \phi_{-n}^*$, with the asterisk denoting the complex conjugate.

Using this expansion in (6), it is clear that the Fourier modes $\phi_n(r,t)$ satisfy the radial wave equation

$$\frac{1}{c^2} \frac{\partial^2 \phi_n}{\partial t^2} = \left[\frac{\partial^2}{\partial r^2} + \frac{1}{r} \frac{\partial}{\partial r} - \frac{n^2}{r^2} \right] \phi_n, \quad r \geqslant R, \ t \geqslant 0, \tag{9}$$

$$\phi_n(r,0) = 0, \quad \frac{\partial \phi_n}{\partial t}(r,0) = 0, \quad r \geqslant R. \tag{10}$$

A general solution to (9) for outgoing waves may be expressed as

$$\phi_n(r,t) = \mathscr{L}^{-1}[a_n(s)K_n(z)](t),$$

where K_n are modified Bessel functions of the third kind (see, e.g., [42]), a_n are arbitrary functions, $\mathscr{L}$ denotes the Laplace transform, and $\mathscr{L}^{-1}$ denotes the inverse Laplace transform. Here s is the dual of the time variable t, and $z = rs/c$. Based on the above, it is easily shown that *exact* non-reflecting boundary condition is given by [29,30]:

$$\frac{\partial \phi}{\partial r} + \frac{1}{c} \frac{\partial \phi}{\partial t} + \frac{1}{2r} \phi = \sum_{n=-\infty}^{\infty} \int_0^t \sigma_n(t-\tau) \phi_n(r,\tau) \, d\tau e^{in\theta}, \quad r = R, \tag{11}$$

with non-reflecting boundary kernel

$$\sigma_n(t) = \frac{1}{r} \mathscr{L}^{-1} \left[z + \frac{1}{2} + z \frac{K_n'(z)}{K_n(z)} \right](t). \tag{12}$$

This history dependent exact condition depends on the time convolution of a kernel which involves the inverse Laplace transform of the logarithmic derivative of K_n

$$\frac{d}{dz} \log K_n(z) = \frac{K_n'(z)}{K_n(z)}. \tag{13}$$

Alpert et al. [31] use uniform rational approximates of the logarithmic derivatives (13) as a ratio of polynomials from which the convolution kernel σ_n can be expressed as a sum of decaying exponentials. In this form, the time convolution integral may be evaluated recursively, and the work per time step and storage is proportional to the number of exponentials used. For large n, the computation may be evaluated rapidly using only $O(\log n)$ pole evaluations per time step. This requires the numerical construction of the poles and coefficients via nonlinear least squares. In [31], the nonlinearity and poor conditioning difficulties of the least squares problem are addressed by linearization and application of Gram–Schmidt orthogonalization. A two-dimensional numerical example using a similar rational approximation for a planar non-reflecting boundary kernel is reported in [4,32]: Numerical results show significantly improved accuracy over Berenger-type PMLs. Numerical examples for the rational approximation of the circular or spherical non-reflecting boundary kernel given in [31] have not as yet been reported in the open literature.

An alternative method for approximating the non-reflecting boundary kernel is to represent it as finite continued fraction. For a spherical boundary in 3D, the non-reflecting boundary kernel can be represented exactly as a finite continued fraction which allows for localization as solutions to a sequence of recursive differential equations [4,28]. In [28], the derivation of the recursive sequence was motivated by the reformulation in [33] of asymptotic boundary conditions based on progressive wave expansions first used in [13]. Finite element implementation of this sequence of local operators in harmonic form, together with a clear relationship to the implementations in [20–22], is given in [27]. In this paper, we use a similar harmonic implementation of the sequence of local boundary operators derived in [28], based on the asymptotic progressive wave expansion for the 2D wave equation on a circle.

In 2D, an approximate solution to (9) may be represented by the progressive wave expansion [34] – the time-domain counterpart to the radial asymptotic (multipole) expansion for $r \to \infty$:

$$\phi_n(r,t) \sim \hat{\phi}_n(r,t) = \sum_{k=0}^{\infty} r^{-k-1/2} \phi_n^k(r-ct). \tag{14}$$

Substituting (14) into (9), gives the recursion relation for the expansion coefficients (wave functions):

$$(\phi_n^k)' = \frac{(k-1/2)^2 - n^2}{2k} \phi_n^{k-1}, \tag{15}$$

where ϕ_n^0 is arbitrary. In general this series does not converge at any fixed r, yet provides a useful representation with particularly good approximation when $z = sr/c \gg n$ (see [4] for estimates of this type).

3.1. Construction of radiation boundary conditions

In the following, we rederive the recursive sequence of local RBCs given in [28], and then reformulate in terms of Fourier modes. We provide a systematic approach for deriving this recursive sequence based directly on the hierarchy of local operators of Bayliss and Turkel [13] which annihilate radial terms in the expansion (14). On a circle, the hierarchy is easily constructed using product of radial derivatives:

$$B_p = L_p(L_{p-1}(\cdots(L_2(L_1)))), \quad L_p = \left(\frac{1}{c}\frac{\partial}{\partial t} + \frac{\partial}{\partial r} + \frac{2p-3/2}{r}\right). \tag{16}$$

Direct application of this product form $B_p[\phi_n]$, involves high order radial derivatives which limits the order p, which can be practically implemented in a numerical method. Inspired by [28], we reformulate the Bayliss and Turkel boundary operators as a recursive sequence involving first-order derivatives only for each mode. This sequence is then cast as a system of first-order differential equations in time, for each harmonic, which may be easily implemented in a numerical method. In this approach, the remainders of the Bayliss and Turkel operators (16) acting on the progressive wave expansion (14) are interpreted as a sequence of auxiliary functions with reduced radial order.

Following Hagstrom and Hariharan [28], the sequence begins by applying the first-order Bayliss operator $B_1 = L_1$ to (14), with residual w_n^1

$$B_1[\hat{\phi}_n] = \left(\frac{1}{c}\frac{\partial}{\partial t} + \frac{\partial}{\partial r} + \frac{1}{2r}\right)\hat{\phi}_n = w_n^1. \tag{17}$$

The function w_n^1 defines the remainder of the radial wave expansion

$$w_n^1(r,t) = \sum_{k=1}^{\infty} -k r^{-k-3/2} \phi_n^k. \tag{18}$$

As noted in [13], $w_n^1(r,t) = \mathrm{O}(r^{-2})\hat{\phi}_n \sim \mathrm{O}(r^{-5/2})$. If we set $w_n^1 = 0$, then $B_1\hat{\phi}_n = 0$. Applying the Fourier expansion to this result evaluated at $r = R$, gives, $B_1[\hat{\phi}] = 0$, on Γ, which defines the first-order local boundary condition of Bayliss and Turkel.

Applying the local operators L_j, $j = 2, \ldots$ to (18) will reduce the order of the remainder further. For example, applying $B_2 = L_2(L_1)$ to (14), we have

$$B_2[\hat{\phi}_n] = \left(\frac{1}{c}\frac{\partial}{\partial t} + \frac{\partial}{\partial r} + \frac{5}{2r}\right)(B_1\hat{\phi}_n) = L_2(w_n^1) = w_n^2 \tag{19}$$

with remainder

$$w_n^2(r,t) = \sum_{k=2}^{\infty} k(k-1) r^{-k-5/2} \phi_n^k. \tag{20}$$

We note $w_n^2(r,t) = O(r^{-4})\hat{\phi}_n \sim O(r^{-9/2})$. Setting $w_n^2 = 0$ and applying the Fourier expansion defines the second-order local boundary condition of Bayliss and Turkel, $B_2 = [\hat{\phi}] = 0$ on Γ.

In general, applying B_{j+1} to (14), we have by induction

$$B_{j+1}[\hat{\phi}_n] = \left(\frac{1}{c}\frac{\partial}{\partial t} + \frac{\partial}{\partial r} + \frac{2j+1/2}{2r} \right)(B_j[\hat{\phi}_n]) = L_{j+1}(w_n^j) = w_n^{j+1}, \tag{21}$$

where w_n^j is defined as

$$w_n^j(r,t) = \sum_{k=j}^{\infty} a_k^j r^{-k-j-1/2}\phi_n^k \tag{22}$$

with coefficients

$$a_k^j = (-1)^j k(k-1)\cdots(k-(j-1)) = (-1)^j \frac{k!}{(k-j)!} \tag{23}$$

We note $w_n^j(r,t) = O(r^{-2j})\hat{\phi}_n = O(r^{-2j-1/2})$.

For $j = 0$, we rewrite (17) as

$$L_1(w_n^0) = \left(\frac{1}{c}\frac{\partial}{\partial t} + \frac{\partial}{\partial r} + \frac{1}{2r} \right)w_n^0 = w_n^1, \tag{24}$$

where

$$w_n^0(r,t) = \sum_{k=0}^{\infty} a_k^0 r^{-k-1/2}\phi_n^k = \hat{\phi}_n(r,t).$$

For $j = 1, 2, \ldots, p_n$ we eliminate radial derivatives in (21) in favor of a recursive sequence for w_n^j. To this end we rewrite

$$L_{j+1}(w_n^j) = \left(\frac{1}{c}\frac{\partial}{\partial t} + \frac{\partial}{\partial r} + \frac{2j+1/2}{r} \right)w_n^j = w_n^{j+1},$$

as

$$\frac{1}{c}\frac{\partial w_n^j}{\partial t} = \frac{1}{2}w_n^{j+1} - \frac{j}{r}w_n^j - \frac{1}{2}\left(\frac{\partial}{\partial r} + \frac{1}{2r} - \frac{1}{c}\frac{\partial}{\partial t} \right)w_n^j. \tag{25}$$

Now consider the last term in the brackets,

$$\left(\frac{\partial}{\partial r} + \frac{1}{2r} - \frac{1}{c}\frac{\partial}{\partial t} \right)w_n^j = \sum_{k=j}^{\infty} a_k^j r^{-k-j-1/2}\{2(\phi_n^k)' - (k+j)r^{-1}\phi_n^k\}. \tag{26}$$

Substituting the recursion relation for $(\phi_n^k)'$ given in (15), and the definition for a_k^i given in (23), into (26) leads to

$$\left(\frac{\partial}{\partial r} + \frac{1}{2r} - \frac{1}{c}\frac{\partial}{\partial t} \right)w_n^j = -\frac{(j-1/2)^2 - n^2}{r^2}\sum_{k=j-1}^{\infty} a_{j-1}^k r^{-k-j+1/2}\phi_n^k = -\frac{(j-1/2)^2 - n^2}{r^2}w_n^{j-1} \tag{27}$$

Using this key result in (25) defines the following recursive sequence for the functions $w_n^j(r,t)$, $j = 1, 2, \ldots, p_n$:

$$\frac{1}{c}\frac{\partial w_n^j}{\partial t} = \frac{(j-1/2)^2 - n^2}{2r^2}w_n^{j-1} - \frac{j}{r}w_n^j + \frac{1}{2}w_n^{j+1} \tag{28}$$

with $w_n^0 = \phi_n$.

Rescaling the variables by 2^{1-j}, applying a Fourier expansion to (24) and (28), with $\phi_n \sim \hat{\phi}_n$, and using the relation

$$\frac{\partial^2}{\partial\theta^2} e^{in\theta} = -n^2 e^{in\theta}$$

we rederive the recursive sequence of local RBCs given by Hagstrom and Hariharan [28]:

$$\left(\frac{1}{c}\frac{\partial}{\partial t} + \frac{\partial}{\partial r} + \frac{1}{2r}\right)\phi = v_1, \tag{29}$$

$$\left(\frac{1}{c}\frac{\partial}{\partial t} + \frac{j}{r}\right)v_j = \frac{1}{4r^2}\left((j-1/2)^2 + \frac{\partial^2}{\partial\theta^2}\right)v_{j-1} + v_{j+1} \tag{30}$$

and

$$v_j(r,\theta,t) = 2^{1-j}\sum_{n=-\infty}^{\infty} w_n^j(r,t)e^{in\theta} \tag{31}$$

for $j = 1, 2, \ldots, p$, and $v_0 = 2\phi$. Here $v_j(R,\theta,t) \in \mathbb{R}$ are 2π-periodic functions satisfying $v_j(R,0,t) = v_j(R,2\pi,t)$.

With p auxiliary functions $\{v_1, v_2, \ldots, v_p\}$, then $v_{p+1} = 0$ and $B_{p+1}[\hat{\phi}] = 0$, with accuracy of order $\sim O(r^{-2p-1/2})$; i.e., the local radiation boundary condition (29), together with the recursive sequence of p first-order differential equations (30), is equivalent to the $p+1$ order Bayliss and Turkel local boundary condition. For example, if only one auxiliary equation is solved for v_1, then v_2 is set to zero, and the radiation boundary condition is equivalent to the second-order boundary condition $B_2\phi = 0$.

The key property of the Hagstrom and Hariharan recursive sequence of differential equations for auxiliary functions is the case in which they may be implemented in a numerical method. Here, the second-order tangential derivatives for the auxiliary functions at the boundary can be conveniently implemented directly in a finite difference scheme [28], or weakly through a finite element method with standard C^0 interpolation (see Section 7 in this paper for implementation details). Alternatively, we can reformulate and implement in integro-differential form using the Fourier expansion (31) together with the efficient computation of the inverse Fourier transform (8).

3.2. Fourier expansion form of radiation boundary conditions

Here, we recognize that when evaluated on the artificial boundary at $r = R$, the sequence (28) forms a system of first-order ordinary differential equations in time for the auxiliary functions, $v_{n,j}(t) = 2^{1-j}w_n^j(R,t) \in \mathbb{C}$, with $v_{n,j} = v_{-n,j}^*$. Let $\mathbf{v}_n(t) = \{2^{1-j}w_n^j(R,t)\}$, $j = 1, 2, \ldots, p_n$, and define a time-dependent vector function of order p_n

$$\mathbf{v}_n(t) = [v_{n,1}(t), v_{n,2}(t), \ldots, v_{n,p_n}(t)]^{\mathrm{T}}$$

then the first-order system of equations may be written as a matrix differential equation for each Fourier mode similar to the exact and asymptotic implementations for a sphere given in [27]

$$\frac{\mathrm{d}}{\mathrm{d}t}\mathbf{v}_n(t) = \mathbf{A}_n\mathbf{v}_n(t) + \phi_n(R,t)\mathbf{b}_n. \tag{32}$$

Here, we have p_n auxiliary functions for the nth harmonic. The constant $p_n \times p_n$, tri-diagonal matrix $\mathbf{A}_n = \{A_n^{ij}\}$, is defined with band

$$\mathbf{A}_n = \frac{c}{R}B\left[\frac{(i-1/2)^2 - n^2}{4R}, -i, R\right], \tag{33}$$

i.e.,

$$
A_n^{ij} = \frac{c}{R} \begin{cases} R & \text{if } i = j - 1, \\ -i & \text{if } i = j, \\ [(i - 1/2)^2 - n^2]/4R & \text{if } i = j + 1, \\ 0 & \text{otherwise.} \end{cases}
$$

The constant vector $\boldsymbol{b}_n = \{b_n^j\}$ is defined by

$$
\boldsymbol{b}_n = \frac{c}{8R^2}(1 - 4n^2)\boldsymbol{e}_1, \tag{34}
$$

where $\boldsymbol{e}_1$ is the unit vector, $\boldsymbol{e}_1 = [1, 0, \ldots, 0]^{\mathrm{T}}$.

We then define the reformulated boundary condition by taking the Fourier expansion of (24), i.e., multiplying by $e^{in\theta}$, summing over n, and evaluating on the truncation boundary Γ

$$
\left(\frac{1}{c}\frac{\partial}{\partial t} + \frac{\partial}{\partial r} + \frac{1}{2r}\right)\phi = \sum_{n=-\infty}^{\infty} v_{n,1}(t)e^{in\theta}, \quad r = R, \tag{35}
$$

where the component $v_{n,1}(t) = w_n^1(R, t) \in \mathbb{C}$, $v_{n,1} = v_{-n,1}^*$, satisfies for each mode, n, the first-order matrix system (32), with initial condition $\boldsymbol{v}_n(0) = 0$, and driven by the radial modes $\phi_n(R, t)$ defined by the Fourier transform (8) evaluated at $r = R$. Here, we recognize that the time convolution given in the exact radiation condition (11) is approximated by the system of differential equations for the auxiliary functions $v_{n,j}(t)$.

In practice, the infinite sum over n in (35) is truncated at a finite value N, i.e., we write the partial sum at $r = R$

$$
B_1[\phi] = \sum_{n=-N}^{N} v_{n,1}(t)e^{in\theta} = v_{0,1} + \sum_{n=1}^{N}[v_{n,1}^c \cos n\theta + v_{n,1}^s \sin n\theta], \tag{36}
$$

where $v_{n,1}^c = 2\mathrm{Re}(v_{n,1})$, and $v_{n,1}^s = -2\mathrm{Im}(v_{n,1}), n = 1, 2, \ldots, N$. Here the auxiliary function $v_1(R, \theta, t)$ is approximated by a trigonometric polynomial of degree N with orthogonal basis

$$
\mathcal{T}_N = \{1, \cos\theta, \cos 2\theta, \ldots, \cos N\theta, \sin\theta, \sin 2\theta, \ldots, \sin N\theta\}.
$$

The finite number of functions $v_{n,1}$ included is equal to the dimension $N_T = \dim(\mathcal{T}_N) = 2N + 1$. For modes $n > N$, (35) reduces to $B_1[\phi] = 0$. For modes $n \leqslant N$, the auxiliary functions satisfy the property, $v_{n,j+1} = \mathrm{O}(R^{-2})v_{n,j}$, so that $v_{n,j+1} < v_{n,j}$, and $v_{n,j} \sim \mathrm{O}(R^{-2j-1/2})$. The total number of auxiliary variables $\boldsymbol{v}_n = \{v_{n,j}\}, j = 1, 2, \ldots, p_n, n = -N, \ldots, -1, 0, 1, \ldots, N$, with fixed upper limit $p_n = P$, is $N_P + \mathrm{O}(N_T P)$. The work per time step and storage required to solve (32) is thus proportional (with a small constant) to $N_P = \mathrm{O}(N_T P)$. In the following we denote this truncated boundary condition by RBCI(N, P), where N defines the number of terms included in the mode series, and $P \leqslant N$ defines the number of auxiliary equations included in (32), for each mode n.

3.3. Stability

The stability of the ordinary differential equation (32) is determined by the eigenvalues of the matrix $\boldsymbol{A}_n$. To obtain a normalized coefficient matrix which is independent of R, we rescale the functions $y_{n,j} = R^j v_{n,j}$, so that the sequence (28) becomes

$$
\frac{R}{c}\frac{\mathrm{d}}{\mathrm{d}t}y_{n,j} = \frac{(j - 1/2)^2 - n^2}{4}y_{n,j-1} - jy_{n,j} + y_{n,j+1} \tag{37}
$$

or in matrix form

$$
\frac{\mathrm{d}}{\mathrm{d}t}\boldsymbol{y}_n(t) = \boldsymbol{C}_n\boldsymbol{y}_n(t) + R\phi_n(R, t)\boldsymbol{b}_n, \tag{38}
$$

where $y_{n,j}, j = 1, 2, \ldots, p_n$ are the elements of the vector $\boldsymbol{y}_n$, and $\boldsymbol{C}_n = \{C_n^{ij}\}$, is a $p_n \times p_n$, *normalized* tridiagonal matrix with band

$$\boldsymbol{C}_n = \frac{c}{R} B \left[\frac{(i-1/2)^2 - n^2}{4}, -i, 1 \right].$$

In this form, the eigenvalue λ_n, may readily be calculated from

$$(\boldsymbol{C}_n - \lambda_n \boldsymbol{I}) \boldsymbol{y}_n = \boldsymbol{0}.$$

We have verified numerically that the eigenvalues (roots) of $\boldsymbol{C}_n$, lie strictly in the left half of the complex plane for $p_n = 1, 2, \ldots, n$, and $n \leqslant 20$. In Fig. 2, the maximum real part of the eigenvalues of the $p_n \times p_n$ matrices $\boldsymbol{C}_n$ are plotted as a family of curves for $n = 1, 2, \ldots, 20$, and $p_n \leqslant n$. The values for $p_n < n$ are bounded by the solid curve representing the maximum eigenvalues computed with $p_n = n$. Results for values $n > 20$ are expected to follow this same trend. Since the maximum real part of the eigenvalues are negative, in fact, $\max(\mathrm{Re}[\lambda_n]) < -1$, solutions to the first-order system of equations for the auxiliary functions are stable.

3.4. Modified radiation boundary condition

To improve the approximation to the truncated harmonics $n > N$, without affecting the modes $n \leqslant N$, we define a modified boundary condition using (21) for $j = 1$, and $r = R$, i.e., applying the second-order Bayliss and Turkel operator, with remainder

$$B_2[\phi_n(R, t)] = 2v_{n,2}(t) \tag{39}$$

we form the expansion

$$B_2[\phi] = 2 \sum_{n=-\infty}^{\infty} v_{n,2}(t) \mathrm{e}^{in\theta}, \quad \text{on } \Gamma, \tag{40}$$

where the function $v_{n,2}(t) = w_n^2(R, t)/2$ satisfies the same first-order matrix system (32), for each harmonic (8).
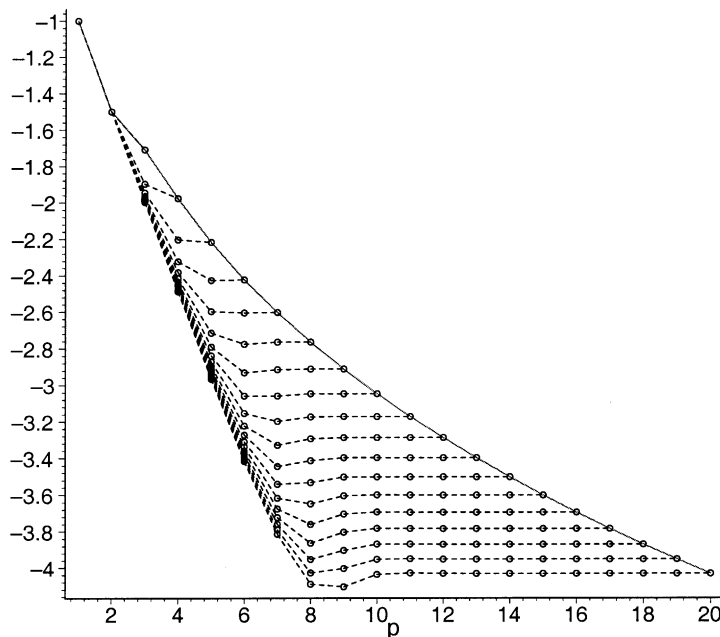

Fig. 2. Maximum real part of eigenvalues for the $p_n \times p_n$ matrix $\boldsymbol{C}_n$ normalized with c/R, vs. dimension p_n. The graph shows a family of dashed curves for $n = 1, 2, \ldots, 20$, and $p_n \leqslant n$. The values are bounded by the solid curve representing the eigenvalues computed with $p_n = n$.

Following a similar procedure to that described in [25,35], the modified boundary condition (40) can be implemented in a symmetric finite element variational equation by introducing additional auxiliary functions $q_n(t)$, $\psi_1(\theta, t)$, and $\psi_2(\theta, t)$, such that

$$B_1[\phi] - \frac{1}{8r}\psi_1 - \frac{1}{2r}\frac{\partial^2 \psi_2}{\partial \theta^2} = r \sum_{n=-\infty}^{\infty} q_n(t)e^{in\theta}, \quad r = R, \tag{41}$$

$$\mathcal{H}[\psi_1] = \phi, \quad \mathcal{H}\left[\frac{\partial^2 \psi_2}{\partial \theta^2}\right] = \frac{\partial^2 \phi}{\partial \theta^2}, \quad r = R, \tag{42}$$

$$\mathcal{H}[q_n(t)] = v_{n,2}(t) \tag{43}$$

with initial conditions, $\psi_1(\theta, 0) = \psi_2(\theta, 0) = 0$, $q_n(0) = 0$, and where

$$\mathcal{H} := \left(\frac{R}{c}\frac{\partial}{\partial r} + 1\right).$$

Eqs. (41)–(43), define an equivalent form of the radiation boundary condition (40), suitable for implementation in a symmetric finite element formulation; the three-dimensional counterpart is formulated in [25–27]. Using the truncation given in (88), we denote our modified radiation boundary condition by RBC2(N, P), where N defines the number of terms included in the truncated series, and $P \leqslant N$ defines the maximum number of auxiliary equations included in (32). Numerical studies of this modified condition compared to RBC1 will be reported in a future manuscript.

4. Finite element implementation

In the following, we give the finite element formulation for the initial-boundary value problem within the bounded computational region Ω, supplemented by the radiation boundary condition (35) on Γ. Extensions for the formulation of the modified condition (40) follows the procedures described in [25,26].

4.1. Variational equation

Under the usual regularity conditions, the statement of the weak form for the initial-boundary value problem in the computational domain Ω may be stated as:
Given load data $f, \alpha, \beta, \gamma, c$ and initial conditions.
Find $\phi(\mathbf{x}, t)$, $\mathbf{x} \in \Omega \cup \partial\Omega$, such that for all admissible weighting functions $\bar{\phi}$, the following variational equation is satisfied:

$$M_\phi\left(\bar{\phi}, \frac{\partial^2 \phi}{\partial t^2}\right) + C_\phi\left(\bar{\phi}, \frac{\partial \phi}{\partial t}\right) + K_\phi(\bar{\phi}, \phi) = F_S(\bar{\phi}) + F_\Gamma(\bar{\phi}) \tag{44}$$

with

$$M_\phi(\bar{\phi}, \phi) := \int_\Omega \frac{1}{c^2}\bar{\phi}\phi \, d\Omega, \tag{45}$$

$$C_\phi(\bar{\phi}, \phi) := \int_S \frac{\beta}{\alpha}\bar{\phi}\phi \, d\mathscr{S} + \int_\Gamma \frac{1}{c}\bar{\phi}\phi \, d\Gamma, \tag{46}$$

$$K_\phi(\bar{\phi}, \phi) := \int_\Omega \nabla\bar{\phi} \cdot \nabla\phi \, d\Omega + \int_S \frac{\gamma}{\alpha}\bar{\phi}\phi \, d\mathscr{S} + \frac{1}{2R}\int_\Gamma \bar{\phi}\phi \, d\Gamma, \tag{47}$$

$$F_S(\bar{\phi}) := \int_\Omega \bar{\phi}f \, d\Omega + \int_\mathscr{S} \bar{\phi}\frac{g}{\alpha} \, d\mathscr{S}, \tag{48}$$

$$F_\Gamma(\bar\phi) := \sum_{n=-\infty}^{\infty} v_{n,1} \int_\Gamma \bar\phi e^{in\theta} \, d\Gamma. \tag{49}$$

In the above, $v_{n,1}$ satisfies the system of first-order differential equations (32), driven by the modes $\phi_n(R, t)$ computed from (8), i.e., the Fourier transform of ϕ on the circular boundary Γ.

For the scattering problem, a known incident wave $\phi^{(i)}(\boldsymbol{x}, t)$ is scattered from the surface $\mathscr{S}$. The total solution ϕ, is then the superposition of the incident wave $\phi^{(i)}$ and scattered field $\phi^{(s)}$, i.e., $\phi = \phi^{(i)} + \phi^{(s)}$. The scattered field is a solution to the wave equation subject to the radiation boundary condition (35) and the surface condition (3):

$$\alpha \frac{\partial \phi^{(s)}}{\partial n} + \beta \frac{\partial \phi^{(s)}}{\partial t} + \gamma \phi^{(s)} = g_s(\boldsymbol{x}, t), \quad \boldsymbol{x} \in \mathscr{S}, \ t \in [0, T], \tag{50}$$

where

$$g_x(\boldsymbol{x}, t) = g - \alpha \frac{\partial \phi^{(i)}}{\partial n} - \beta \frac{\partial \phi^{(i)}}{\partial t} - \gamma \phi^{(i)}. \tag{51}$$

For a given $\phi^{(i)}$ the scattered field may be solved within Ω using the weak form of the IBVP defined in (44), with ϕ and g replaced with $\phi^{(s)}$ and g_s, respectively. We note that this solution requires normal derivatives of the time-dependent incident wave, $\partial \phi^{(i)}/\partial n$, appearing in (51). For complex surfaces, the computation of normal derivatives may be inconvenient.

An alternative formulation which avoids explicitly computing derivatives on $\mathscr{S}$ is derived by exploiting the separable form of the circular radiation boundary and solving for the total field ϕ. In order to directly solve ϕ within Ω, the variational equation is modified to represent the incident wave field on the radiation theory Γ. The scattered field is then computed by subtracting the give incident wave from the total field, i.e., $\phi^{(s)} = \phi - \phi^{(i)}$. To solve for the total field, we modify the linear operator F_Γ as

$$F_\Gamma(\bar\phi) := \sum_{n=-\infty}^{\infty} v_{n,1} \int_\Gamma \bar\phi e^{in\theta} \, d\Gamma + \int_\Gamma \bar\phi B_1[\phi^{(i)}] \, d\Gamma, \tag{52}$$

where B_1 is the first-order local operator of Bayliss and Turkel, and $v_{n,1}(t)$ is a solution of the first-order system:

$$\frac{d}{dt} \boldsymbol{v}_n(t) = \boldsymbol{A}_n \boldsymbol{v}_n(t) + \boldsymbol{b}_n \phi_n^{(s)}(R, t) \tag{53}$$

driven by modes,

$$\phi_n^{(s)}(R, t) = \frac{1}{2\pi R} \int_\Gamma e^{-in\theta} [\phi(R, \theta, t) - \phi^{(i)}(R, \theta, t)] \, d\Gamma. \tag{54}$$

In this formulation, normal derivatives of the incident wave are not computed on the surface $\mathscr{S}$. Instead, the incident wave is represented on the circular radiation boundary Γ, where the normal derivative reduces to the radial derivative, $\partial \phi^{(i)}/\partial n = \partial \phi^{(i)}/\partial r$, which is easily computed.

4.2. Finite element discretization

To obtain a finite element approximation to the solution of the variational equation (44), the domain $\bar\Omega$ is discretized into a finite number of subdomains (elements), and we apply the standard Galerkin semi-discrete approximation

$$\phi(\boldsymbol{x}, t) \approx \phi^h(\boldsymbol{x}, t) = \boldsymbol{N}(\boldsymbol{x}) \boldsymbol{d}_\phi(t), \tag{55}$$

$$\bar\phi(\boldsymbol{x}, t) \approx \bar\phi^h(\boldsymbol{x}, t) = \boldsymbol{N}(\boldsymbol{x}) \bar{\boldsymbol{d}}_\phi(t), \tag{56}$$

where $N(x)$ is a row vector of standard C^0 basis functions with compact support associated with each node, and $d_\phi(t)$ is a time-continuous column vector containing the nodal values of ϕ^h. The superscript h denotes a finite-dimensional basis. Using the approximation in (44), we arrive at the following system of second-order ordinary differential equations in time:

$$M_\phi \ddot{d}_\phi(t) + C_\phi \dot{d}_\phi(t) + K_\phi d_\phi(t) = f(t), \quad t > 0, \tag{57}$$

$$d_\phi(0) = \phi_0, \quad \dot{d}_\phi(0) = \dot{\phi}_0. \tag{58}$$

In the above, M_ϕ, C_ϕ and K_ϕ are standard symmetric, sparse arrays associated with the finite element discretization of the wave equation and the local B_1 operator; and $f(t) = f_S + f_\Gamma$ is the discrete force vector composed of a standard load vector f_S and a part associated with the auxilliary functions appearing in the radiation boundary condition.

From (49) it is clear that the force vector takes the form

$$f_\Gamma(t) = R \sum_{n=0}^{N}{}' [v_{n,1}^c(t) f_n^c + v_{n,1}^s(t) f_n^s], \tag{59}$$

where the prime on the sum indicates that a factor of 1/2 multipliers the term with $n = 0$, and

$$f_n^c := \int_0^{2\pi} N^{\mathrm{T}}(\theta) \cos n\theta \, \mathrm{d}\theta, \quad f_n^s := \int_0^{2\pi} N^{\mathrm{T}}(\theta) \sin n\theta \, \mathrm{d}\theta. \tag{60}$$

In (59), the functions $v_{n,1}^c$ and $v_{n,1}^s$ are the first element of the vector arrays $v_n^c = \{v_{n,j}^c\} = 2\mathrm{Re}(v_n)$, and $v_n^s = \{v_{n,j}^s\} = 2\mathrm{Im}(v_n)$, which satisfy the system of first-order differential equations (32) driven by the even and odd radial modes at $r = R$, i.e.,

$$\frac{\mathrm{d}}{\mathrm{d}t}[v_n^c(t)] = A_n v_n^c(t) + \phi_n^c(R,t) b_n, \quad n = 0, 1, 2, \ldots, N,$$
$$\frac{\mathrm{d}}{\mathrm{d}t}[v_n^s(t)] = A_n v_n^s(t) + \phi_n^s(R,t) b_n, \quad n = 0, 1, 2, \ldots, N \tag{61}$$

with inner products,

$$\phi_n^c(R,t) = \frac{1}{\pi} f_n^{cT} \phi_\Gamma(t), \quad \phi_n^s(R,t) = \frac{1}{\pi} f_n^{sT} \phi_\Gamma(t). \tag{62}$$

In the above, $\phi_\Gamma(t) = \{\phi_A(t)\}$, $A = 1, 2, \ldots, N_\Gamma$, is a vector of nodal values evaluated on the artificial boundary Γ with N_Γ nodes.

4.3. Efficient implementation

The radiation boundary condition only requires inner products of trig functions and finite element basis functions with compact support within the boundary vectors f_n^c and f_n^s. To save computation, these vectors may be computed in closed form for each boundary element and assembled (gather operation). The global vectors f_m, $m = 1, 2, \ldots, N_T$, may then be organized in order and stored by column in the matrix $F = [f_1, f_2, \ldots, f_{N_T}]$, of dimension $(N_\Gamma \times N_T)$, with coefficients $[F_{Am}] = \{f_A\}_{,m}$. In this case, we write

$$f_\Gamma(t) = RF v_{,1}(t), \quad \phi(t) = F^{\mathrm{T}} \phi_\Gamma(t),$$

where $v_{,1} = \{v_m\}_{,1}$ and $\phi(t) = \{\phi_m(R,t)\}$. Using this construction, the matrix-vector products can be computed efficiently using Level-2 BLAS, with storage requirements and number of operations $\mathrm{O}(N_\Gamma N_T)$. Typically, the total number of harmonics required is less than the number of nodes on the boundary $N_T = 2N + 1 < N_\Gamma$, by a factor of five or more. Thus, the work required for the computation of the inner products $\mathrm{O}(N_\Gamma N_T)$ is less than the work of $\mathrm{O}(N_\Gamma^2)$ required for the explicit finite element calculation in the interior of the domain.

Alternatively, the cosine and sine functions may be approximated by a projection onto the finite-dimensional basis. In particular, the Fourier modes may be approximated by the interpolant using the expansion

$$\cos n\theta \approx \boldsymbol{N}(\theta)\boldsymbol{y}_n^c, \quad \sin n\theta \approx \boldsymbol{N}(\theta)\boldsymbol{y}_n^s, \tag{63}$$

where $\boldsymbol{y}_n^c = \{\cos n\theta_A\}$, $\boldsymbol{y}_n^s = \{\sin n\theta_A\}$, $A = 1, 2, \ldots, N_\Gamma$, are vectors containing the nodal values of the nth mode on Γ.

Using this expansion in (59) we have

$$\boldsymbol{f}_\Gamma(t) = R\boldsymbol{M}_\Gamma \sum_{n=0}^{N} {}'[v_{n,1}^c(t)\boldsymbol{y}_n^c + v_{n,1}^s(t)\boldsymbol{y}_n^s], \tag{64}$$

where $v_{n,1}^c$ and $v_{n,1}^s$ are driven by

$$\phi_n^c(R, t) = \frac{1}{\pi}\boldsymbol{y}_n^{cT}\boldsymbol{M}_\Gamma\boldsymbol{\phi}_\Gamma(t), \quad \phi_n^s(R, t) = \frac{1}{\pi}\boldsymbol{y}_n^{sT}\boldsymbol{M}_\Gamma\boldsymbol{\phi}_\Gamma(t). \tag{65}$$

In the above, $\boldsymbol{M}_\Gamma = [M_{AB}]$ is the $N_\Gamma \times N_\Gamma$ symmetric/sparse matrix

$$\boldsymbol{M}_\Gamma := \int_0^{2\pi} \boldsymbol{N}^\mathrm{T}\boldsymbol{N}\,\mathrm{d}\theta.$$

This matrix may be diagonalized using nodal (Lobatto) quadrature, e.g., with linear interpolation, $M_{AB} = (1/2)(\theta_{A+1} - \theta_{A-1})\delta_{AB}$. To reduce storage costs further, the vector $\boldsymbol{f}_\Gamma(t) = \{f_A(t)\}$ in (64) may be computed efficiently using the dot-product form:

Algorithm 4.1 (*Matrix-vector product for force vector $\boldsymbol{f}_\Gamma$*).
　　For $A = 1$ to N_Γ
　　　　$f_A(t) = v_{0,1}(t)/2$
　　　　For $n = 1$ to N,
　　　　$f_A(t) = f_A(t) + v_{n,1}^c(t)\cos n\theta_A + v_{n,1}^c(t)\sin n\theta_A$
　　　　End
　　　　$f_A(t) = f_A(t) \cdot M_A \cdot R$
　　End.
where $M_A = \mathrm{diag}(\boldsymbol{M}_\Gamma)$, and the harmonics $\{\cos n\theta\}$ and $\{\sin n\theta\}$ for a given node point A, are calculated using the recurrence relations:

$$\begin{aligned}
\cos n\theta_A &= \cos(n-1)\theta_A \cos\theta_A - \sin(n-1)\theta_A \sin\theta_A, \\
\sin n\theta_A &= \sin(n-1)\theta_A \cos\theta_A + \cos(n-1)\theta_A \sin\theta_A.
\end{aligned} \tag{66}$$

Similarly, the computation of $\phi_n(R, t)$ in (65) is performed efficiently using the linear combination of columns form for matrix-vector products, together with the trig recursive relation (66), e.g.,

Algorithm 4.2 (*Matrix-vector product for Fourier modes*).
　$\boldsymbol{\phi} = 0$
　For $A = 1$ to N_Γ,
　　$\phi_A(t) = \phi_A(t) \cdot M_A/\pi$
　　For $n = 0$ to N,
　　$\phi_n^c(R, t) = \phi_n^c(R, t) + \phi_A(t)\cos n\theta_A$
　　$\phi_n^s(R, t) = \phi_n^s(R, t) + \phi_A(t)\sin n\theta_A$
　　End
　End.

Using trig function recursion and the above algorithms, the number of operations required to perform the inner products remains $\mathrm{O}(N_\Gamma N_T)$, while the storage requirements are reduced to $\mathrm{O}(N_\Gamma)$ words. In [36],

similar use of trig recursion was used to compute the matrix-vector products required for an iterative solution with the complex DtN map on a circle for the Helmholtz equation.

Setting $\phi_n = (\phi_n^c - i\phi_n^s)/2$, and $v_{n,1} = (v_{n,1}^c - iv_{n,1}^s)/2$, we recognize that up to a constant, the above algorithms for the inner-products form the discrete Fourier transform of $\phi(R, \theta, t)$, and the inverse discrete Fourier transform for $v_1(R, \theta, t)$, respectively:

$$\phi_n(R, t) = \frac{1}{2\pi} \sum_{\theta_A \in \Gamma} \phi_A(t) \cdot M_A \mathrm{e}^{-in\theta_A}, \quad n = -N, \dots, N,$$

$$f_A(t) = RM_A \sum_{n=-N}^{N} v_{n,1}(t) \mathrm{e}^{in\theta_A}, \quad \theta_A \in \Gamma.$$

When the number of functions in the series expansion $N_T = 2N + 1$ is increased to be the same as the number of points on Γ, i.e., $(N_T = N_\Gamma)$, then for uniform grid spacing $\theta_A = A\Delta\theta$ on Γ, the Fast Fourier Transform (FFT) may be used to compute the inner products, with number of operations $\mathrm{O}(N_\Gamma \log N_\Gamma)$ – still less than the work $\mathrm{O}(N_\Gamma^2)$ required for the explicit finite element calculation in the interior domain Ω. Recently, FFT algorithms have also been developed for non-uniformly spaced data, see [37], allowing for efficient computation on non-uniform grids θ_A.

For both trig recursion and the FFT algorithms, the work and storage is less than the $\mathrm{O}(N_\Gamma^2)$ work required for the finite element calculation in the interior domain. We note that the work per time step and storage associated with calculation of the auxiliary functions in (61) is proportional to $N_p = \mathrm{O}(N_T P)$, independent of the number of points used on the boundary Γ. Typically, $P \ll N_T$, and the work and storage is negligible compared to the work and storage required to calculate the finite element equations and Fourier transforms.

Similar finite element implementations with efficient calculation of Fourier transforms may be used for the rational approximations to the non-reflecting boundary kernel as a sum of poles given in [31]. In that case, the boundary conditions are uniformly convergent a fixed r, and the function $v_{n,1}(t)$ in the convolution (36) would be replaced by a summation over other auxiliary functions $z_{n,j}(t)$ satisfying a similar first order system of differential equations (32) with the real-valued coefficients in A_n and b_n replaced with complex pole coefficients α_{nj} and pole locations β_{nj}, $\mathrm{Re}(\beta_{nj}) \leqslant 0$, (see Table 2 in [31] for a listing of the poles for the first four modes $n = 1, 2, 3, 4$).

4.4. Time-integration

Since the form of (59) or (64) and (61), are similar to the implementation of RBCs on a sphere given in [22], similar time-integration algorithms may be used to advance the solution. As discussed in [22], one time-integration approach is to apply the explicit central difference method directly to (57). The equations may be decoupled using standard diagonal mass M, and damping matrices C, e.g. using nodal quadrature, row-sum technique, or the HRZ lumping scheme. The stability condition for the central difference method with lumped mass is $\Delta t \leqslant h/\sqrt{2}c$, where Δt is the time step, h is the smallest element size in a 2-D finite element mesh. This method requires the forcing term $f^k = f(t_k)$ at time step $t_k = k\Delta t$ be available. Therefore, to update the solution $d^{k+1} = d_\phi(t_{k+1})$, only the evaluation of $v_n^k = v_n(t_k)$ is needed. To numerically solve (61), either the explicit second-order Adams–Bashforth method or the the implicit second- order Adams–Moulton method (trapezoidal rule) may be used. The computational work required in solving is negligible, since the matrices A_n, are banded, relatively small, and remain constant. The stability condition imposed on Δt by the Adams–Bashforth method depends on the eigenvalues λ_n of the coefficient matrix A_n that is $-1 \leqslant \lambda_n \Delta t \leqslant 0$ with critical time step:

$$\Delta t < \frac{1}{|\min(\mathrm{Re}\lambda_n)|}. \tag{67}$$

As shown in Fig. 3, $|\min(\mathrm{Re}\lambda_n)|$ increases with dimension n. Values for $p_n < n$ are bounded by the values for $p_n = n$. For a fixed c/R, the critical time step decreases when more terms N are included in the non-reflecting boundary condition. However, for a given mesh and N, the stability constraint on Δt imposed by
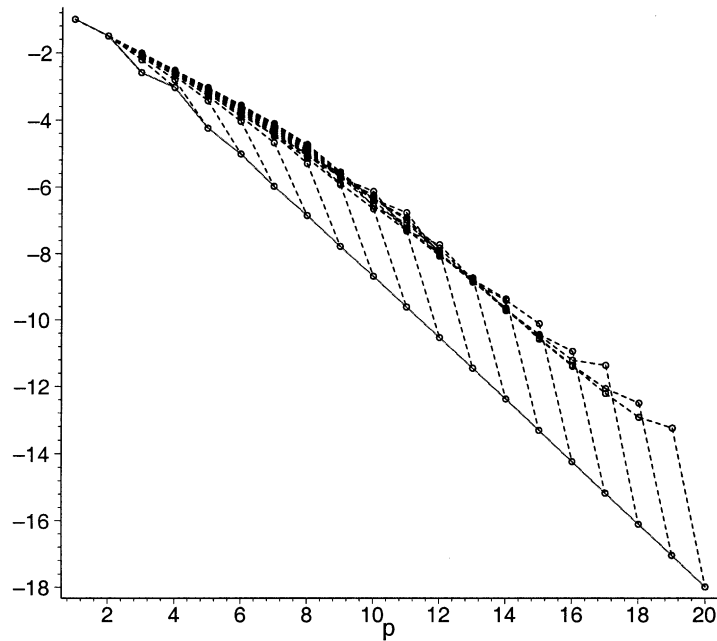
Fig. 3. Minimum real part of eigenvalues for the $p_n \times p_n$ matrix $\boldsymbol{C}_n$ normalized with c/R, vs. dimension p_n. The graph shows a family of dashed curves for $n = 1, 2, \ldots, 20$, and $p_n \leqslant n$. The values are bounded by the solid curve representing the eigenvalues computed with $p_n = n$.

the explicit central difference method applied to (57) is generally more restrictive than the explicit Adams–Bashforth method applied to (61).

An alternative approach is to apply the Newmark family of algorithms (and variations such as HHT-α) in predictor/corrector form to the semi-discrete equations (57), see [22]. Any of the members of the Newmark family may be used, including the second-order accurate and unconditionally stable trapezoidal rule, and conditionally stable central difference method. The solution of the Newmark algorithm requires the forcing term $\boldsymbol{f}^{k+1}$, and therefore $\boldsymbol{v}_n^{k+1}$. In this case the value $\boldsymbol{v}_n^{k+1}$, may be computed concurrently using an explicit time-integrator applied to (61); e.g., the explicit second-order accurate Adams–Bashforth algorithm. Complete algorithms for computing the solution concurrently with auxiliary functions on Γ, using either implicit or explicit time integrators, are given in [22].

5. Computation of far field solutions

In [24], a method is described for efficient calculation of far field solutions in 3D. Here, we use a similar method for the two-dimensional wave equation with the recursive sequence of local boundary operators. At each discrete time step, radial modes computed on a circular artificial boundary which drive the radiation condition for the near-field solution, are imposed concurrently as data for the radial wave equation in the far-field. The radial grid is truncated at the far-field point of interest with the modal form of the radiation boundary condition. The solution in the far-field is then computed from an inverse Fourier transform of the radial modes.

The far-field solution is the extension of $\phi(\boldsymbol{x}, t)$ for $r = \|\boldsymbol{x}\| \geqslant R$, in $\mathscr{D}$. With the source $f(\boldsymbol{x}, t)$ and initial data confined to the bounded domain Ω, then in the exterior region $\mathscr{D}$, the scalar field $\phi(\boldsymbol{x}, t)$ satisfies the homogeneous form of the wave equation (4), driven by the near-field solution evaluated at $r = R$.

In order to efficiently compute the far-field solution in $\mathscr{D}$, we transform the problem using the Fourier expansion (7) and apply the radiation boundary condition (35) expressed in modal form at a point $r = R_0$, where $R < R_0 < \infty$:

$$B_1\phi_n|_{r=R_0} = z_{n,1}(t). \tag{68}$$

In the above, B_1 is the first-order local operator and $z_{n,1}$ is the first component of the vector function $z_n(t)$, where $z_n(t)$ is the solution to the matrix differential equation (32) with R, replaced by R_0.

Using (7) and (68), the extension of the the near-field solution on the circular boundary Γ, to the far-field $\mathscr{D}$, reduces to solving the modes $u(r,t) = \sqrt{r}\phi_n(r,t)$, for $n \geqslant 0$, in the region $R \leqslant r \leqslant R_0$. Each mode $n = 0,\ldots,N$. satisfies the following modified radial wave equation with the homogeneous initial data, and driven by the near-field solution evaluated at $r = R$:

$$\left[\frac{1}{c^2}\frac{\partial^2}{\partial t^2} - \frac{\partial^2}{\partial r^2} + \frac{4n^2-1}{4r^2}\right]u(r,t) = 0, \quad r \in (R,R_0), \ t \in \mathbb{R}^+, \tag{69}$$

$$u(r,0) = 0, \quad r \in (R,R_0), \tag{70}$$

$$\frac{\partial u}{\partial t}(r,0) = 0, \quad r \in (R,R_0), \tag{71}$$

$$u(R,t) = \sqrt{R}\phi_n(R,t), \quad t \in \mathbb{R}^+, \tag{72}$$

$$\left(\frac{\partial}{\partial r} + \frac{1}{c}\frac{\partial}{\partial t}\right)u(R_0,t) = \sqrt{R_0}z_{n,1}(t), \quad t \in \mathbb{R}^+ \tag{73}$$

and $z_{n,1}(t)$ satisfies (32), with R, replaced by R_0. In practice, we restrict $-N \leqslant n \leqslant N$, and the solution at any point in physical space, (r,θ), for $r \in (R,R_0)$ is recovered from the Fourier expansion (7) truncated at the finite value N:

$$\phi(r,\theta,t) = \sum_{n=-N}^{N} \phi_n(r,t)e^{in\theta}. \tag{74}$$

Based on the asymptotic properties of the local boundary operators, i.e., $z_{n,j} \sim \mathrm{O}(R_0^{-2j-1/2})$, in the far-field with $R_0 > R$, a fewer number of equations P are required to obtain accurate solutions. Furthermore, the RBC reduces to the local B_1 boundary operator in the asymptotic limit $R_0 \to \infty$; i.e., in the asymptotic limit, the remainder $z_{n,1}(t) \sim 0$, and the RBC for each mode tends to the local B_1 condition

$$\left(\frac{\partial}{\partial r} + \frac{1}{c}\frac{\partial}{\partial t}\right)u(r,t) = 0, \quad r \to \infty. \tag{75}$$

Thus if the far-field point is sufficiently distant from the source of radiation, the RBC may be simplified a priori to the local B_1 condition.

5.1. Space-time discretization for the far-field

The non-reflecting boundary condition (73) involves first-order derivatives only and can be implemented easily into numerical methods. Let u_j^k denote the approximation of $u(r_j,t_k)$ where $r_j = R + j\Delta r$, and $t_k = k\Delta t$. For each mode n, the radial wave equation (69) may be approximated using the central difference operator for both $u_{,tt}$ and $u_{,rr}$, and with u, averaged about u_j^k:

$$\frac{(u_j^{k+1} - 2u_j^k + u_j^{k-1})}{(c\Delta t)^2} = \frac{(u_{j+1}^k - 2u_j^k + u_{j-1}^k)}{(\Delta r)^2} - (4n^2 - 1)\frac{(u_{j+1}^k + 2u_j^k + u_{j-1}^k)}{(4r_j)^2}. \tag{76}$$

Using the method of characteristics, we set $\Delta r = c\Delta t$, so that (76) specializes to the second-order explicit difference scheme for $j = 1,2,\ldots,l-1$:

$$u_j^{k+1} = u_{j+1}^k + u_{j-1}^k - u_j^{k-1} - (4n^2 - 1)\left(\frac{\Delta r}{4r_j}\right)^2(u_{j+1}^k + 2u_j^k + u_{j-1}^k). \tag{77}$$

To ensure outgoing waves, we truncate the exterior grid at the finite radius, $r_l = R + l\Delta r = R_0$, and impose the radiation boundary condition (73). Using a simple difference formula for $u_{,r}$ and $u_{,t}$ centered at $j = l$, and setting $\Delta r = c\Delta t$ gives

$$u_{l+1}^k = u_l^{k-1} - u_l^{k+1} + u_{l-1}^k - 2\Delta r \sqrt{R_0} z_{n,1}(t_k). \tag{78}$$

Substituting (78) into (77) evaluated at $j = l$, and after rearranging, we obtain

$$u_l^{k+1} = u_{l-1}^k - \frac{(4n^2-1)\Delta r^2}{32R_0^2 - (4n^2-1)\Delta r^2}\left(u_{l-1}^k + 2u_l^k + u_l^{k-1}\right) + 2\Delta r\sqrt{R_0}\left[1 - \frac{16R_0^2}{32R_0^2 - (4n^2-1)\Delta r^2}\right]z_{n,1}(t_k). \tag{79}$$

To solve the system of equations (32) for the auxiliary functions $v_n(t)$, the second-order accurate, and unconditionally stable, Adams–Moulton method (trapezoidal rule) may be used

$$(\boldsymbol{I} - \alpha \boldsymbol{A}_n)\boldsymbol{z}_n^{k+1} = (\boldsymbol{I} + \alpha \boldsymbol{A}_n)\boldsymbol{z}_n^k + \alpha(\phi_n(R_0, t_{k+1}) + \phi_n(R_0, t_k))\boldsymbol{b}_n. \tag{80}$$

In the above, $\boldsymbol{z}_n^k = \boldsymbol{z}_n(t_k)$, and $\alpha = \Delta r/2c$.

In [24], we developed time-integration algorithms for computing the far-field solution *concurrently* with the near-field solution in 3D without saving lengthy time-history data at interior points. The same time-stepping algorithm applies to the 2D problem described herein. At each discrete time step, the Fourier modes $\phi_n(R, t) = R^{-1/2}u(R, t)$ evaluated on the boundary $r = R$, and used for the near-field RBC are imposed concurrently as boundary data for the radial wave equation in the far-field $r > R$. Using an implicit method for the interior and explicit method for the auxiliary functions on the boundary at $r = R$, the following algorithm may be used to update the far-field solution:

1. Compute the modal solutions $\phi_n(R, t_k)$ and $\phi_n(R, t_{k-1})$ at time steps t_k and t_{k-1} using the tangential Fourier transform (8).
2. Update the near-field solution by first calculating the auxiliary variables $v_n(t_{k+1})$ using the explicit Adams–Bashforth algorithm for the first-order system (32). Then calculate the interior solution $\boldsymbol{d}_\phi(t_{k+1})$ using the Newmark predictor/corrector algorithm for the second-order symmetric system (57).
3. Update the exterior modal solution $\phi_n(r_j, t_{k+1})$ using the difference equations (77) and (79). Then update $z_{n,1}(t_{k+1})$ using (80).
4. Recover the far-field solution $\phi(r_j, \theta, t_{k+1})$ using the Fourier expansion (74).

The above algorithm only requires saving the interior solution at the current and previous time steps.

If the far-field observation points are not known a priori, the Fourier modes computed from the near-field solution, $\phi_n(R, t)$, may be saved for later use. In this case, the computation would be performed in two stages: In the first, the modes $\phi_n(R, t)$ are computed from the near-field solution and saved at each time step. In the second, the preserved functions $\phi_n(R, t)$ are used as time-dependent boundary conditions to extrapolate solutions to the far-field.

6. Numerical studies

Numerical examples are computed to study the accuracy and convergence properties of the asymptotic radiation boundary condition RPC1(N,P) defined in (36), (32) and (88). Comparisons are made to numerical solutions using the local boundary operators B_1 and B_2, and exact steady-state solutions. By comparing transient numerical solutions to the steady harmonic limit as time becomes large, we are able to isolate specific frequencies, which might arise from a time Fourier transform of a transient pulse. Here we use the second-order accurate, implicit trapezoidal rule in predictor/corrector form for the semi-discrete equations (57), together with the explicit second-order accurate Adams–Bashforth algorithm for the first-order system of auxiliary functions (61). The method is demonstrated with three test problems, radiation from a line segment in a circular baffle and scattering from a rigid circular cylinder and a soft elliptic cylinder at oblique incidence. For far-field solutions, we assess the accuracy of the second-order finite difference discretization (77) of the radial wave equation separately for individual modes $\phi_n(r, t)$.

6.1. Transient radiation from a line element on a circular cylinder

Consider time-dependent radiation from a line element on a cylinder with radius $a = 0.5$, such that

$$\phi(a, \theta, t) = f(\theta) \sin \omega t \, H(t), \quad 0 \leqslant \theta \leqslant 2\pi, \ t \geqslant 0, \tag{81}$$

where $H(t)$ is the unit-step (Heaviside) function and

$$f(\theta) = \begin{cases} 1, & 0° \leqslant |\theta| \leqslant \theta_1, \\ \dfrac{|\theta| - \theta_2}{\theta_1 - \theta_2}, & \theta_1 < |\theta| \leqslant \theta_2, \\ 0, & \text{otherwise.} \end{cases} \tag{82}$$

For this example, we set $\theta_1 = 15°$, and $\theta_2 = 30°$. This problem is challenging in that the waves radiated from the vicinity of $\theta = 0°$ are attenuated by a geometric spreading loss as they travel along longitudes down to the south pole $\theta = 180°$. We derive the exact steady-state solution to this problem by expanding the function $f(\theta)$ in a Fourier series, and evaluating the outgoing radiated solution at $r = a$, with the result

$$\phi(r, \theta, t) = -\text{Im} \left\{ e^{-i\omega t} \frac{1}{2\pi} \sum_{n=0}^{\infty} \frac{H_n(kr)}{H_n(ka)} A_n \cos n\theta \right\} \tag{83}$$

with coefficients, $A_0 = \theta_1 + \theta_2$; and for $n \geqslant 1$,

$$A_n = \frac{4}{n^2} \frac{\cos n\theta_2 - \cos n\theta_1}{\theta_1 - \theta_2}. \tag{84}$$

In the above, H_n are cylindrical Hankel functions of the first kind, and $k = \omega/c$ is the wave number (normalized frequency). Since the problem is symmetric, it is sufficient to compute the solution in the domain $\Omega = \{a < r < R, 0 \leqslant \theta < \pi\}$. Using symmetry, only even functions are included in (64)

$$\boldsymbol{f}_\Gamma(t) = \sum_{n=0}^{N} {}' v_{n,1}^c(t) \boldsymbol{M}_\Gamma \boldsymbol{y}_n^c \tag{85}$$

driven by the Fourier modes on the half-circle

$$\phi_n^c(R, t) = \frac{2}{\pi} \boldsymbol{y}_n^{cT} \boldsymbol{M}_\Gamma \boldsymbol{\phi}_\Gamma(t), \quad \boldsymbol{M}_\Gamma := \int_0^\pi \boldsymbol{N}^{\mathrm{T}}(\theta) \boldsymbol{N}(\theta) \, \mathrm{d}\theta. \tag{86}$$

The circular radiation boundary Γ is positioned at three different locations defined by $R/a = [1.25, 1.5, 1.75]$, with corresponding meshes of $[10, 20, 30] \times 240$ elements evenly spaced in the region $(0.5 \leqslant r \leqslant R) \times (0 \leqslant \theta \leqslant \pi)$. The computation is driven from rest to steady-state with wave speed $c = 1$, a normalized frequency $\omega a/c = \pi$, and a time step $\Delta t = 0.50 \times 10^{-2}$. The element size ($\Delta r = 1.25 \times 10^{-2}$, $a\Delta\theta = 1.15 \times 10^{-2}$, $R\Delta\theta = 0.65 \times 10^{-2}$), and time increment are relatively small so that the error is primarily due to the radiation boundary treatment.

For reference, Fig. 4 shows contours of the numerical solution using $\text{RBC1}(20, 3)$ positioned at $R/a = 1.75$, for a representative time $t = 12$, during steady-state. Fig. 5 shows the solution at the observation point $R/a = 1.75$ and $\theta = 180°$, located in the shadow zone on the backside of the radiating line element. In this difficult region, the solution using B_1 and B_2 exhibits large spurious reflections, while the solution using $\text{RBC1}(20, 3)$ gives accurate solutions.

The instantaneous error $e(t) = \phi^h - \phi$, measured in L_2 norm on a circular boundary with radius $r = \rho_0$ is defined as

$$E(t) = \left\{ \int_0^\pi \left[\phi^h(\rho_0, \theta, t) - \phi(\rho_0, \theta, t) \right]^2 \mathrm{d}\theta \right\}^{1/2}, \tag{87}$$

where ϕ^h is the approximate finite element solution and ϕ is the exact steady-state solution. The maximum L_2 error over a steady-state interval $t \in (t_1, t_2)$ is computed from $E_{\max} = \max_{t_1 \leqslant t \leqslant t_2} E(t)$.
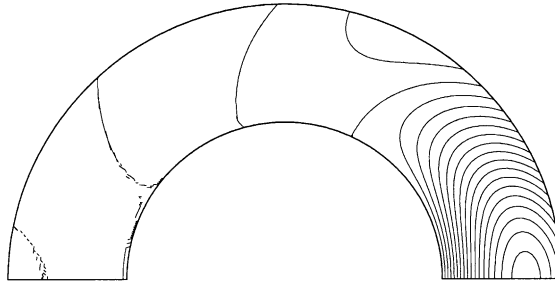
Fig. 4. Radiation from a line element on a cylinder with radius $a = 0.5$ and frequency $\omega a/c = \pi$. Solution contours at steady state $(t = 12)$, using RBC1(N, P), with $N = 20$, and $P = 3$. Radiation boundary Γ set at $R/a = 1.75$.
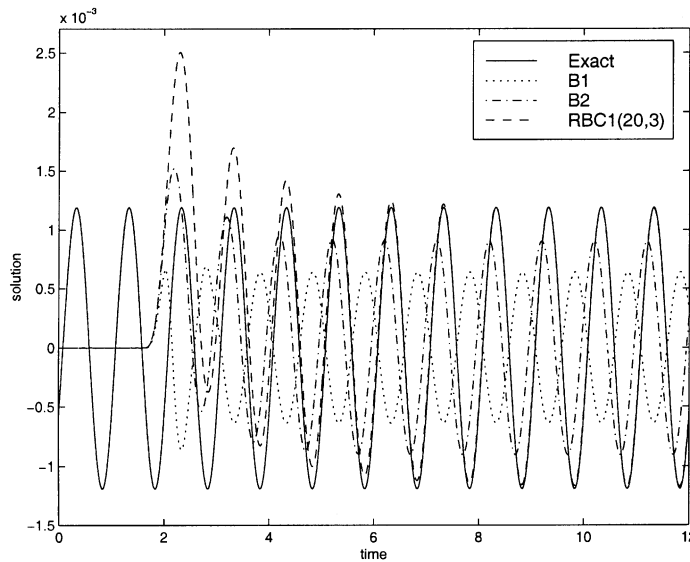

Fig. 5. Time-histories at observation point on $R/a = 1.75$, and $\theta = \pi$.

Fig. 6(a) shows the maximum L_2 error for RBC1$(N, 10)$ measured on a circle with radius $\rho_0/a = 1.25$, when the radiation boundary condition is moved from $R/a = 1.25$ to $R/a = 1.75$, and the number of modes included in the radiation boundary condition N, increasing from 0 to 20. We observe that the solutions using RBC1$(N, 10)$ are rapidly driven to approximately the same minimum error value for each truncation boundary position. This limiting error is controlled by the discretization of the Fourier transforms and interior mesh. As the truncation boundary is moved further away from the source, the number of modes N required to reach the level of the discretization error is reduced. For example, for $R/a = 1.25, N = 20$ terms are needed, whereas, when R/a is increased to 1.75, only $N = 7$ terms are required.

Fig. 6(b) shows the maximum error using RBC1(N, P) for fixed $N = 20$, and with variable $P \leqslant 8$. With the number of grid points on the boundary, $N_\Gamma = 240$, and $N = 20$, then there are $N_\Gamma/N = 12$ angular grid points/mode. These results show that accurate solutions are obtained using a value of P significantly lower than N. In particular, for the case where the truncation boundary Γ, is positioned close to the source at $R/a = 1.25$, such that $N = 20$ modes are needed to reach the level of the discretization error, then $P = 5$ equations are sufficient. In general, we observe that $P \geqslant N/3$ is sufficient to obtain an accurate solution for this problem.

To study the frequency dependence of the asymptotic radiation boundary conditions RBC1(N, P), we vary the normalized frequency between a wide range $2.5 \times 10^{-3} \leqslant \omega a/c \leqslant 10$. Here we use a mesh of (15×120) elements evenly spaced in the region $(0.5 \leqslant r \leqslant R) \times (0 \leqslant \theta \leqslant \pi)$, with fixed time step $\Delta t = 0.01$.
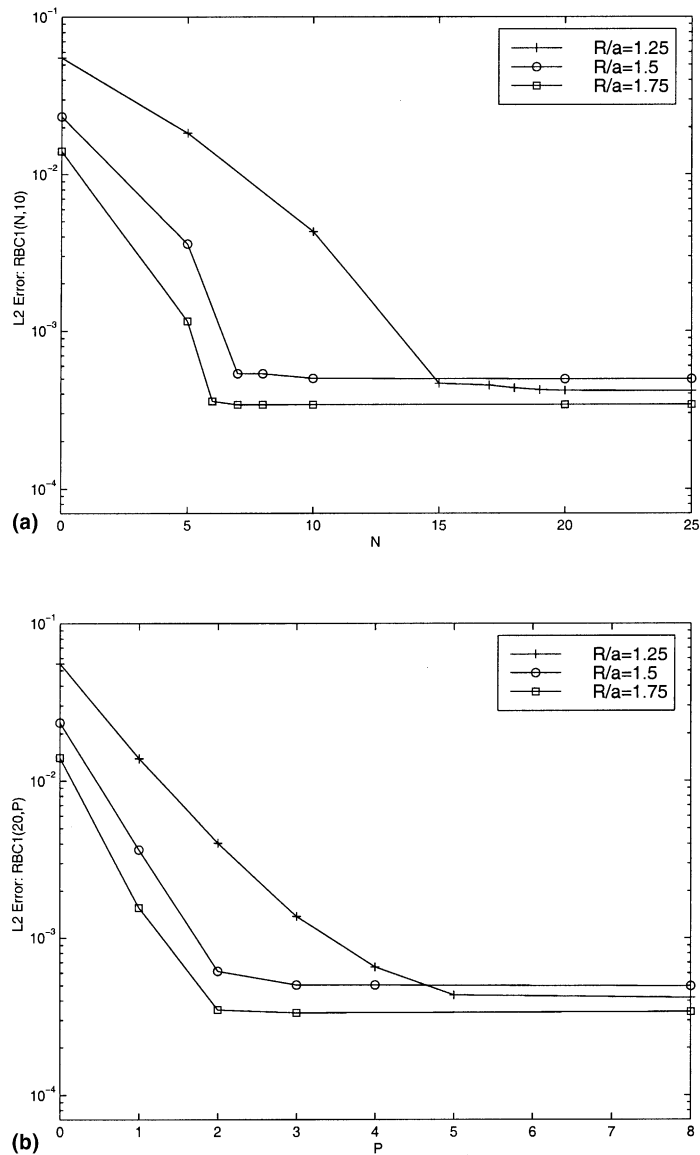
Fig. 6. Radiation from line element on a cylinder of radius $a = 0.5$ and frequency $\omega a/c = \pi$. Maximum L_2 error during steady state measured at $r/a = 1.25$. Radiation boundary condition applied at truncation boundary Γ positioned at $R/a = 1.25$, 1.5, 1.75. Numerical solutions using (a) RBC1$(N, 10)$, (b) RBC1$(20, P)$.

With this mesh, the element lengths are: $\Delta r = 2.5 \times 10^{-2}$, $a\Delta\theta = 1.3 \times 10^{-2}$, $R\Delta\theta = 2.3 \times 10^{-2}$. As the frequency is progressively reduced to smaller values the discretization error becomes negligible (because the solution becomes smoother), and the error is governed by P. Fig. 7 shows the maximum L_2 error on the radiation boundary $R/a = 1.75$, at steady-state with $N = 20$, and $0 \leqslant P \leqslant 6$. Initially, as $\omega a/c$ is reduced from 10 to 1, we rapidly drive down the error with increasing P, to the level of the decreasing discretization error. When $\omega a/c$ is reduced further below 1, the error in the asymptotic radiation boundary condition increases. However even at very low normalized frequencies of the order 10^{-3}, improved accuracy is achieved with increasing P – high-degree of accuracy of the order $O(10^{-3})$ is maintained for $P \geqslant 3$. We note that the lack of convergence to the discretization error in the boundary conditions is exhibited only at very low frequencies. In the low frequency case, accurate solutions may be obtained to any practical order desired by increasing the number of residual functions combined with an expansion of the domain (boundary extension). The use of boundary extension, would however, increase the size of the
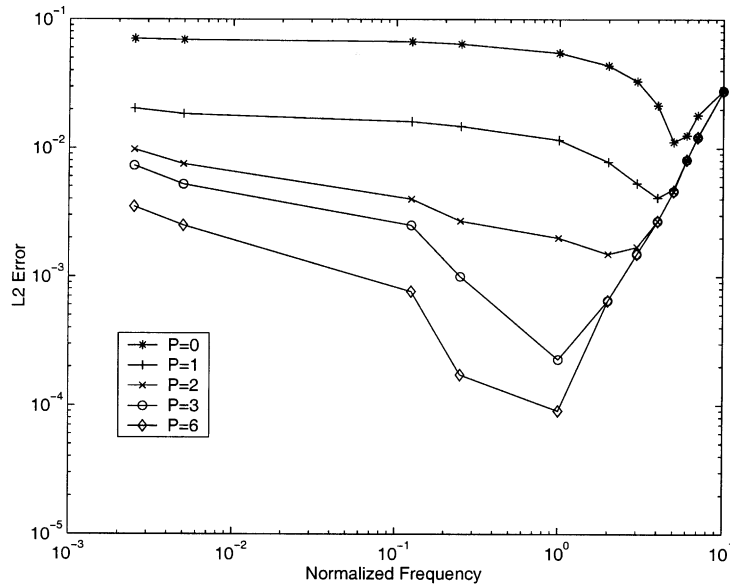
Fig. 7. Radiation from line element on a cylinder. Maximum L_2 error on radiation boundary position $R/a = 1.75$ vs. normalized frequency $\omega a/c$. Numerical solution with RBC1$(20, P)$.

computational domain, and in this low frequency limit, other approximate conditions would be appropriate, such as the double asymptotic approximations (DAA) in [40,41], or the convergent rational approximates in [31].

Due to the rapid reduction in order of the residual functions $v_{n,j}$, it may be sufficient to use a *variable* number of auxiliary variables p_n which is less than the nth model order, i.e. $p_n \leqslant n$. In this case, the number of equations p_n, used in (32), for each mode $|n| \leqslant N$, may be defined by

$$p_n = \begin{cases} |n| & \text{for } |n| < p, \\ P & \text{for } |n| \geqslant P. \end{cases} \tag{88}$$

For $n = 0$, then $p_0 = 0$, so that $v_{0,1} = 0$. With this truncation of the number of auxiliary functions, then the total number of auxiliary functions is

$$N_P = 2 \left[\sum_{n=1}^{P} n + P(N - P) \right] = (2PN - P^2 + P),$$

which is less than the total number $N_P = N_T P$ required for a *fixed* number of variables with $p_n = P$ for all $n = -N, \ldots, -1, 0, 1, \ldots, N$. Fig. 8 shows a comparison of numerical solutions for RBC1(N, P) with a fixed and variable number of auxiliary function p_n for each mode n. Here the mesh is 15×120 with $R/a = 1.25$, $\omega a/c = \pi$, and $\Delta T = 0.01$. The results show that with a fixed number of auxiliary variables $p_n = P$ for each mode n, the solution error is driven to a lower value with increasing P, compared to the variable number defined by (88). With variable p_n, the L_2 error levels out at O(10^{-3}) with no further improvement with increasing P or N, whereas the fixed case is able to reduce the error further to O(10^{-4}). We note however, that the relatively low L_2 errors of order O(10^{-3}) achieved by the variable p_n definition (88) would be acceptable for many applications.

6.2. Transient scattering of a plane wave by a circular cylinder

Consider a cylinder of radius $a = 1$, on which we assume a homogeneous Neumann boundary condition

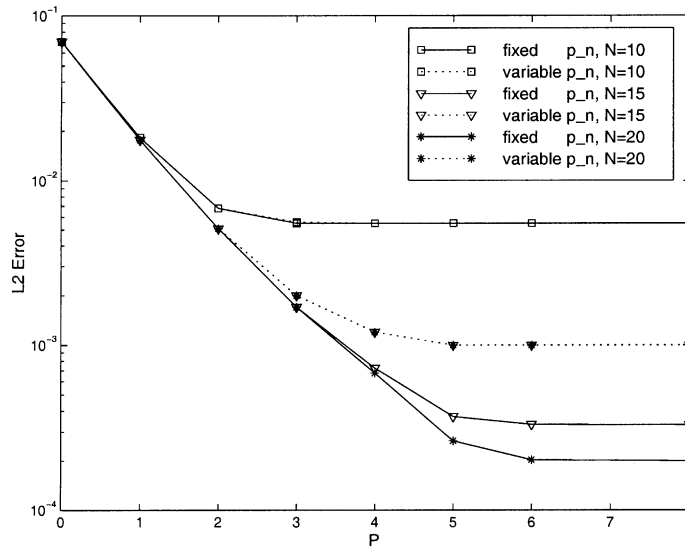$$\frac{\partial \phi}{\partial r} = 0, \quad \text{on } r = a. \tag{89}$$

Fig. 8. Radiation from line element on a cylinder. Maximum L_2 error on radiation boundary position $R/a = 1.25$. Numerical solution with RBC1(N, P) comparing a *fixed* number of auxiliary functions $p_n = P$ for each mode n, with a *variable* number $p_n = |n|$, for $|n| < P$, and $p_n = P$, for $|n| \geqslant P$.

If ϕ is the acoustic pressure, this condition represents a 'rigid' scatterer. Let the incident wave be represented by a traveling place wave along the x-axis at speed c, i.e.,

$$\phi^{(i)} = \begin{cases} \sin[k(x - x_0) - \omega t], & t \geqslant \dfrac{x - z_0}{c}, \\ 0, & t < \dfrac{x - x_0}{c}. \end{cases} \tag{90}$$

Here $k = \omega/c$, and x_0 is the location of the initial wave front at time $t = 0$. The total field $\phi(r, \theta, t)$ is composed of a superposition of the incident wave $\phi^{(i)}(x, t)$ and a scattered wave $\phi^{(s)}(r, \theta, t)$, i.e. $\phi = \phi^{(i)} + \phi^{(s)}$. With the Neumann boundary condition (89), the scattered field is a solution to the wave equation subject to the boundary condition

$$\frac{\partial \phi^{(s)}}{\partial r} = -\frac{\partial \phi^{(i)}}{\partial r} = -k \cos u \cos \theta H \left(t - \frac{x - x_0}{c} \right) \quad \text{on } r = a \tag{91}$$

and $u = k(x - x_0) - \omega t$, $x = a \cos \theta$.

For $\phi^{(i)}$ given in (90), the steady-state analytical solution is

$$\phi^{(s)}(r, \theta, t) = \operatorname{Im} \left\{ e^{-i(kx_0 + \omega t)} \sum_{n=0}^{\infty}{}' A_n H_n(kr) \cos(n\theta) \right\}, \tag{92}$$

$$A_n = -i^n \frac{(2n + 1)}{2} \frac{J_n'(ka)}{H_n'(ka)}. \tag{93}$$

In the above, J_n and H_n are Bessel's and Hankel's functions of the first kind, respectively [42].

The computational domain is discretized with a uniform mesh of standard 4-node bilinear finite elements with 240 evenly spaced elements in $0 \leqslant \theta \leqslant \pi$. The radiation boundary is placed at three different radii $R/a = [1.25, 1.5, 1.76]$, with corresponding mesh $240 \times [10, 20, 30]$. The computation is driven from rest at $x_0 = -2$, to steady-state with $c = 1$, normalized frequency $\omega a/c = \pi$, and time step $\Delta t = 0.01$.

Contours for the scattered solution computed using RBC1$(10, 10)$ positioned at $R/a = 1.75$ are shown in Fig. 9. Fig. 10 shows time-histories of the scattered solution on the artificial boundary Γ defined by $R/a = 1.25$, both at $\theta = 0$, and the backscattered point $\theta = \pi$. At the backscattered point, the solutions using the first and second local operators of Bayliss and Turkel, defined by B_1, B_2, and the asymptotic
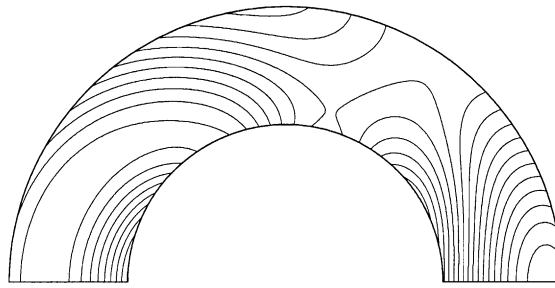
Fig. 9. Scattering from a circular cylinder with wave incident from the ($\theta = \pi$) direction, and normalized frequency $\omega a/c = \pi$. Scattered field contours at steady state using ($t = 15$), using RBC1(10, 10) and $R/a = 1.75$.
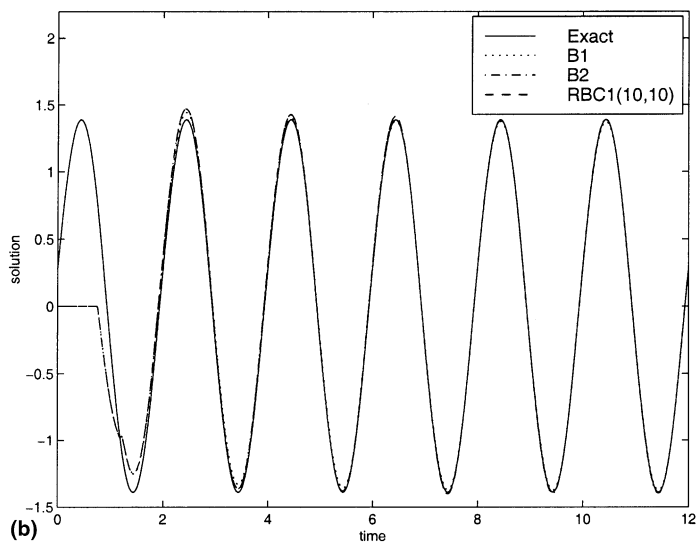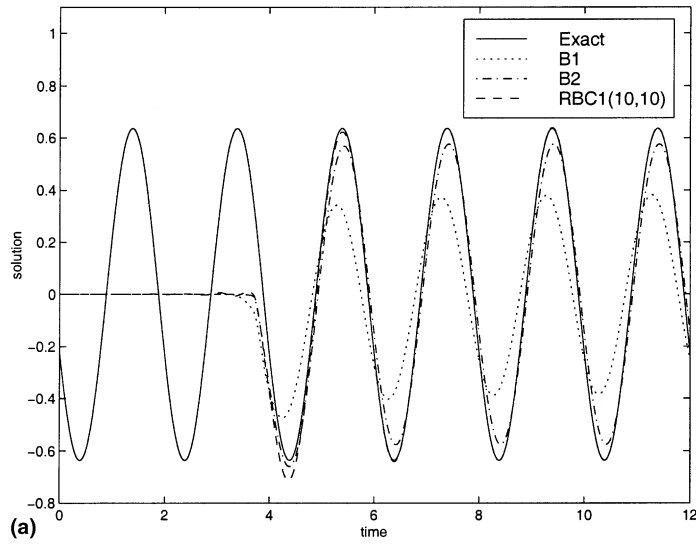

Fig. 10. Scattering of plane-wave from a cylinder. Time-histories on the artificial boundary defined by $R/a = 1.25$, at (a) $\theta = 0$, and (b) backscattered point $\theta = \pi$. Results compared for local operators B_1, B_2 and RBC1(N, P) with $N = P = 10$.

radiation boundary condition RBC1(10, 10) can barely be distinguished from the exact steady-state solution. However, on the other side of the cylinder, at point $\theta = 0$, both operators B_1 and B_2 exhibit significant spurious reflection. In contrast, the solution using RBC1(10, 10) matched the exact solution very well.

Fig. 11 shows the maximum L_2 error during steady-state measured on a cylinder with radius $\rho/a = 1.25$. For this example, we observe that the error in the solution using RBC1(N, 10) are rapidly driven down to the discretization error with increasing N. As the radiation boundary is moved further away from the source, the number of modes N required to obtain a fixed level of accuracy is reduced. For example, for $R/a = 1.25$, $N = 8$ modes are needed to reach the discretization error. As the radiation boundary is moved further away from the scatterer to $R/a = 1.25$, then only $N = 6$ modes are needed. The maximum error using RBC1(N, P) for fixed $N = 8$, and with variable $P \leqslant 6$ is shown in Fig. 11(b). These results again show that the uniform asymptotic approximation to the exact condition is sufficiently accurate with $N/3 \leqslant P \leqslant N$ (see Fig. 12).
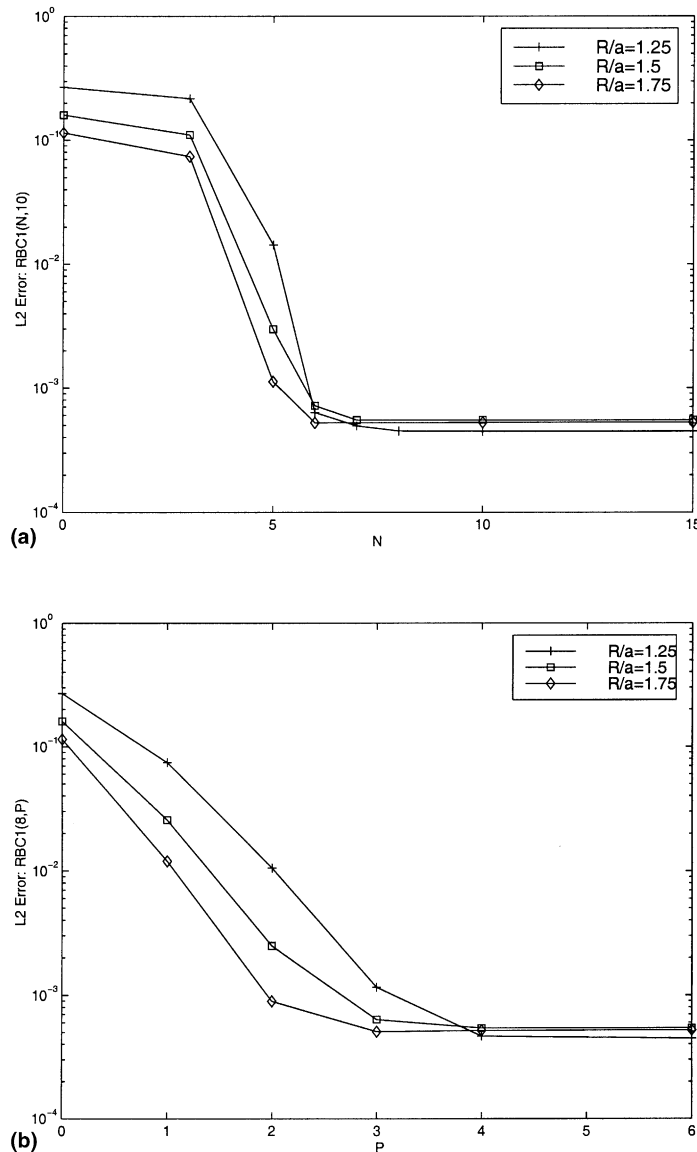

Fig. 11. Scattering of a plane-wave from a circular cylinder. Maximum L_2 error during steady state measured at $r/a = 1.25$. Radiation boundary condition applied at truncation boundary Γ positioned at $R/a = 1.25$, 1.5, 1.75. Numerical solutions using (a) RBC1(N, 10), (b) RBC1(8, P).
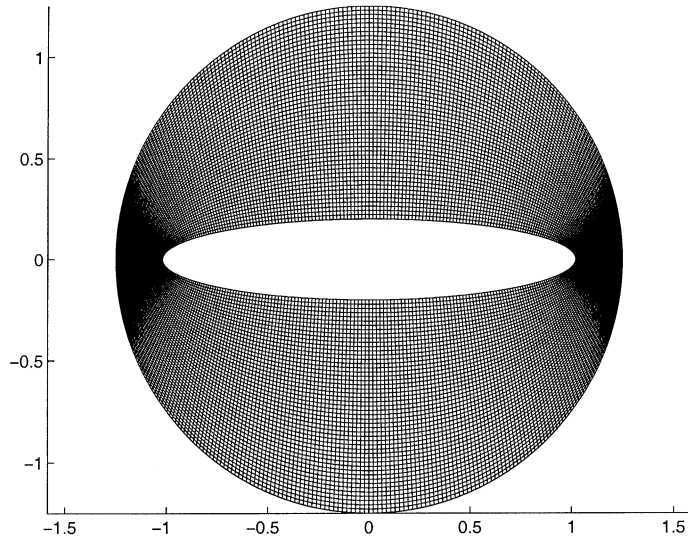
Fig. 12. Finite element mesh for elliptic scatterer defined with foci $f = 1$, $\mu = 0.2$. The circular radiation boundary, Γ, is positioned at $R = 1.25$.

6.3. Transient scattering from an elliptic cylinder

To study the accuracy of the radiation boundary condition for scattering from a non-circular object, we consider the problem of diffraction of an incident plane-wave traveling off-axis to an infinite elliptic cylinder. The ellipse is defined by coordinates $x = f \cosh \mu \cos \theta$, and $y = f \sinh \mu \sin \theta$. Here we choose the radial coordinate $\mu_0 = 0.2$, and foci $f = 1$, resulting in an aspect ratio of major to minor axis of approximately 5:1. The cylinder is assumed infinite in the z-direction, so that the problem can be solved as a two-dimensional problem in the xy-plane.

On the surface of the cylinder, we assume a 'soft' (homogeneous Dirichlet) boundary condition

$$\phi = \phi^{(i)} + \phi^{(s)} = 0 \quad \text{on } \mathscr{S} := \{\mu_0 = 0.1, 0 \leqslant \theta \leqslant 2\pi\}. \tag{94}$$

Here the total field $\phi(\mu, \theta)$ is composed of the incident wave $\phi^{(i)}$, and the scattered wave field $\phi^{(s)}$, such that $\phi^{(s)}(\mu_0, \theta) = -\phi^{(i)}(\mu_0, \theta)$.

The incident plane-wave is given by

$$\phi^{(i)}(\boldsymbol{x}, t) = \sin[k\boldsymbol{v} \cdot (\boldsymbol{x} - \boldsymbol{x}_0) - \omega t] H[t - \boldsymbol{v} \cdot (\boldsymbol{x} - \boldsymbol{x}_0)/c]. \tag{95}$$

Here $\boldsymbol{x}_0 = [x_0, y_0]$ defines the position of the initial wave front at $t = 0$. The direction of the incident plane-wave is determined by the unit wave vector $\boldsymbol{v} = [\cos \alpha, \sin \alpha]$, where α is the angle between the lines of constant phase and the x-axis.

We obtain the exact steady-state solution for the scattered field by expanding the exponential form of the incident wave in elliptic coordinates by means of an addition theorem [43]. For $\phi^{(i)}$ given in (95), and homogeneous boundary condition (94), the steady-state analytical solution is

$$\phi^{(s)}(\mu, \theta, t) = \text{Im}\left\{ \hat{\phi}^{(s)}(\mu, \theta) e^{-i(k\boldsymbol{v} \cdot \boldsymbol{x}_0 + \omega t)}, \right\} \tag{96}$$

where

$$\hat{\phi}^{(s)} = -2 \sum_{n=0}^{\infty} i^n \left\{ A_n Mc_n^{(3)}(\mu, q) ce_n(\theta, q) + B_n Ms_n^{(3)}(\mu, q) se_n(\theta, q) \right\}, \tag{97}$$

$$A_n = \frac{Mc_n^{(1)}(\mu_0, q)}{Mc_n^{(3)}(\mu_0, q)} ce_n(\alpha, q), \quad B_n = \frac{Ms_n^{(1)}(\mu_0, q)}{Ms_n^{(3)}(\mu_0, q)} se_n(\alpha, q).$$

In the above, $q = (kf/2)^2$, ce_n and se_n are the even and odd valued angular Mathieu functions, and $Mc_n^{(p)}$ and $Ms_n^{(p)}$, $p = 1, 3$ are even and odd radial (modified) Mathieu functions of the first and third kind, respectively [42].
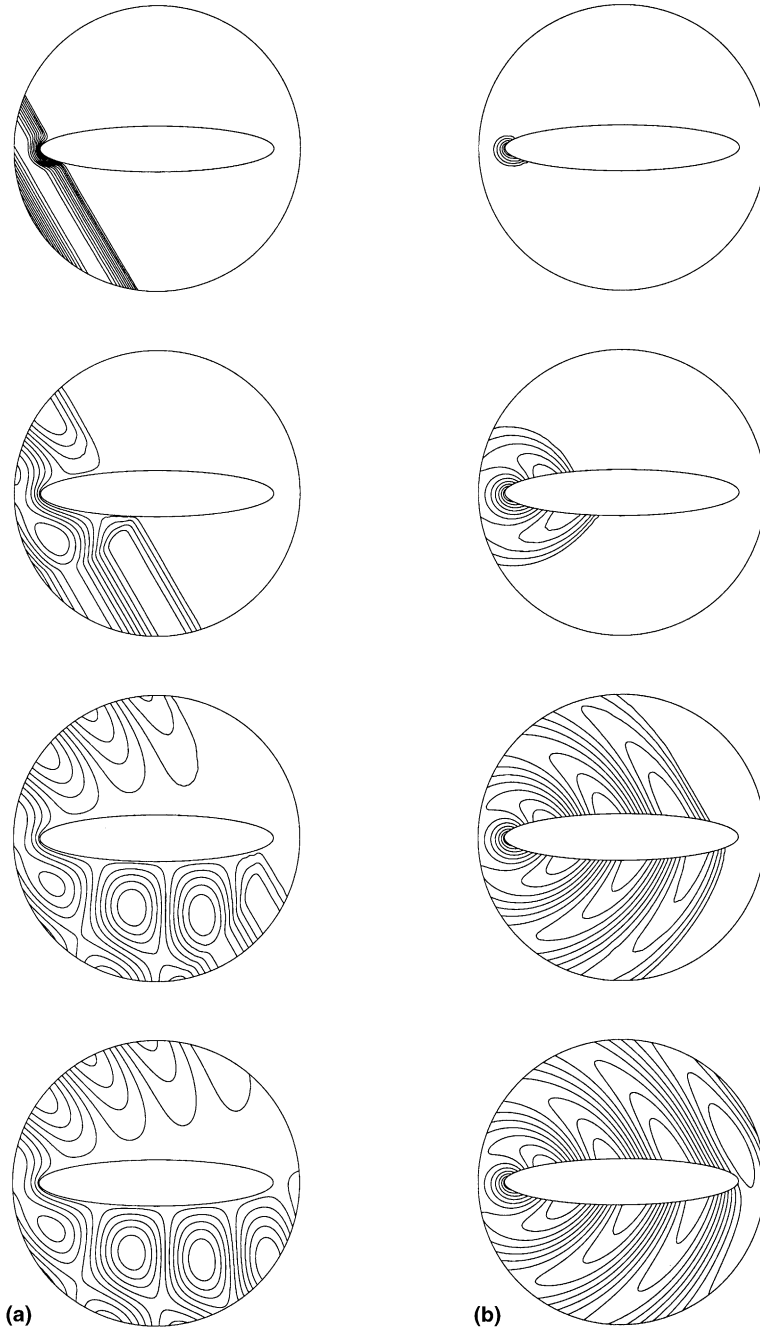

Fig. 13. Scattering from an elliptic cylinder with incident plane-wave oriented in $\theta = 30°$ direction, and normalized frequency $k = \omega/c = 2\pi$. Elliptic scatterer defined with foci $f = 1$, $\mu = 0.2$. Finite element solution contours at time step (50, 100, 200, 500), using RBC1(20, 10) and circular radiation boundary at $R = 1.25$. (a) Total field, (b) scattered field.

For the finite element solution, the radius of the circular radiation boundary Γ is set at $R = 1.25$. The computational domain is discretized with a quasi-uniform mesh of standard 4-node bilinear finite elements with 360 evenly spaced node points on the circular radiation boundary Γ, and 50 node points in the radial direction. The computation is driven from rest to steady-state with wave vector angle $\alpha = 30°$, $c = 1$, frequency $k = \omega/c = 2\pi$, and time step $\Delta t = 0.01$. The initial wave front starts at the radiation boundary, such that $\boldsymbol{x}_0 = -R\boldsymbol{v}$. We use the modified variational equation for the total field, where the incident wave is represented on the circular radiation boundary Γ. For the incident wave defined in (95), the modification to the boundary operator $\boldsymbol{f}_\Gamma$ given in (52) involves the inner product with the local B_1 operator acting on the incident wave: For $t \geqslant R[\cos(\theta - \alpha) + 1]/c$,

$$B_1 \phi^{(i)} = k[\cos(\theta - \alpha) - 1] \cos u + \frac{1}{2R} \sin u, \tag{98}$$

where $u = kR[\cos(\theta - \alpha) + 1] - \omega t$.

Fig. 13 shows finite element solution contours for both total and scattered fields at time steps $(50, 100, 200, 500)$, using the radiation boundary condition $\text{RBC1}(N, P)$ with $N = 20$ angular modes and residual functions defined by $P = 10$. After 50 time steps, the incident plane-wave has just begun to diffract from the elliptic cylinder. After 500 time steps the solution has reached steady-state.

Fig. 14 shows the maximum L_2 error using $\text{RBC1}(N, 20)$ and $\text{RBC1}(20, P)$ during steady-state measured on the circular artificial boundary Γ, positioned at $R = 1.25$. The results show that the number of residual functions defined by P required to reduce the the error to the discretization level is less than the number of modes N needed. For $\text{RBC}(N, 20)$, $N = 18$ is required to reach the discretization error, whereas, for $\text{RBC1}(20, P)$, only $P = 4$ functions are needed.

6.4. Far field calculation for individual modes

In this section we study the accuracy of the asymptotic radiation boundary condition applied to the far-field boundary for individual modes. The radial modes are extrapolated to the far-field using the second-order accurate explicit finite difference algorithm given in (77) and (79). We consider time-harmonic radiation for radial modes at $R = 1.25$, such that

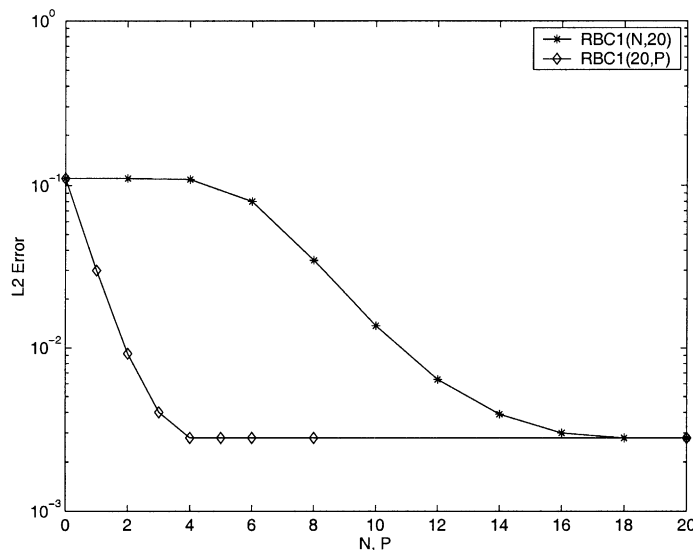$$\phi_n(R, t) = \sin \omega t, \quad t \geqslant 0. \tag{99}$$

Fig. 14. Scattering of a plane-wave from an elliptic cylinder. Maximum L_2 error using $\text{RBC1}(N, 20)$ and $\text{RBC1}(20, P)$ during steady state measured on the circular artificial boundary Γ, positioned at $R = 1.25$.

The exact steady-state solution to the radial wave equation for this problem is

$$\phi_n(r,t) = -\text{Im}\left\{ \frac{H_n(kr)}{H_n(kR)} e^{-i\omega t} \right\}, \quad r \geqslant R, \ t \geqslant t_s, \tag{100}$$

where H_n are Hankel functions of the first kind, $k = \omega/c$ is the wave number (normalized frequency), and t_s is the time after which steady-state has been reached.

For numerical solutions, we set $\omega = 4\pi$, $c = 1$, and time step $\Delta t = 0.005$. The results obtained using the radiation boundary condition at the far field point $r = R_0$ are denoted by RBC1(P), where P denotes for the number of equations included in the first-order system (32), evaluated at R_0. Fig. 15 compare time-dependent solutions obtained using RBC1(3), and the local operator B_1 positioned at the far-field truncation point $R_0/R = 2$. Results are shown for three increasingly higher modes: $n = 0, 10, 20$. For $n = 0$, both B_1 and RBC1(3) solutions match the exact solution very well, as expected. As the mode number increases, the B_1 solution is observed to exhibit both amplitude and phase error at steady state, while RBC1(3) solution can barely be distinguished from the exact solution, even for the relatively high mode number $n = 20$.
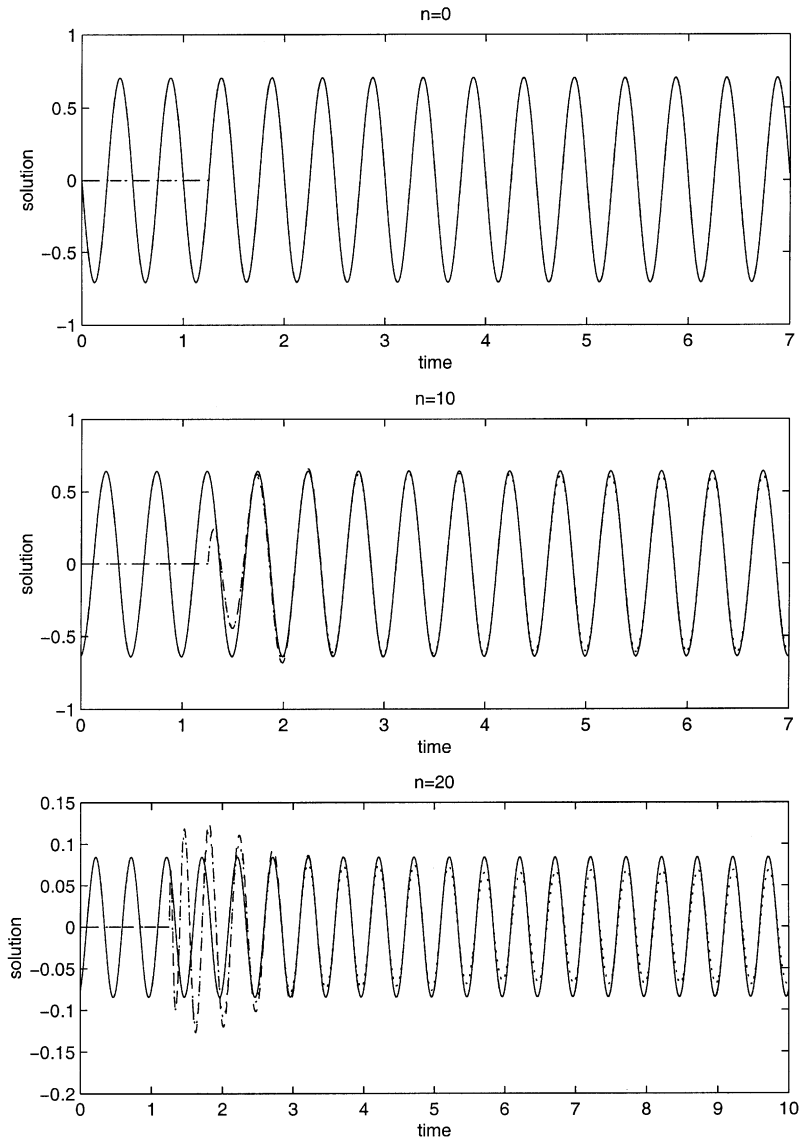

Fig. 15. Comparison of time-dependent solutions for individual modes computed using RBC1(3) and the local B_1 operator, at $kR_0 = 10\pi$. Solid lines denote exact steady-state solution; dashed lines denote RBC1(3); dotted lines denote B_1.
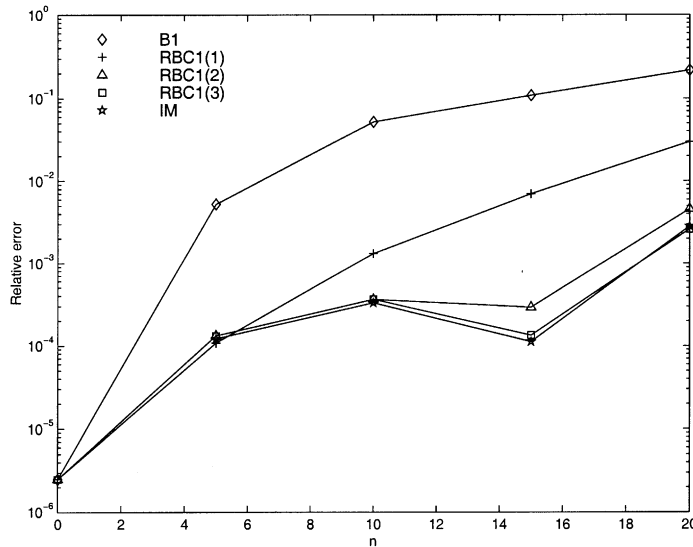
Fig. 16. Relative error versus Fourier mode n. Results are computed using infinite mesh (IM), B_1, and RBC1(P) with $P = 1, 2,$ and 3.

Fig. 16 compares the max relative error, $R(t) = \phi_n^h(R_0, t)/\phi_n(R_0, t) - 1$, at steady-state versus mode n, and $P = 1, 2, 3$. Results are also given for an 'infinite mesh' solution, denoted (IM), obtained by extending the radial discretization to a distant point such that outgoing waves with speed $c = 1$ do not reach the far-field truncation point in the time-interval of interest. The error in the IM solution is caused purely by the finite difference approximation (77) of the radial wave equation. As expected, discretization error for the IM solution generally increases with the mode number n. However, the error for $n \leqslant 20$ are all less than 0.4% which indicate the high accuracy of the finite difference approximation (77) for the current time step. The error in RBC1(P) solution converges to the IM solution, when P, the number of auxiliary functions included, increases from 1 to 3. With $P = 3$, the RBC1 condition gives highly accurate results with the same order of accuracy as the IM solution, but with significant reduction in the size of the mesh.

7. Comparisons to direct implementation of local operators

In this section, we compare the accuracy and efficiency of a direct implementation of the recursive sequence of high-order local boundary operators for the auxiliary functions $v_j(\theta, t)$ given in (29) and (30), repeated here in expanded form:

$$\left(\frac{1}{c} \frac{\partial}{\partial t} + \frac{\partial}{\partial r} + \frac{1}{2R} \right) \phi = v_1(\theta, t), \tag{101}$$

$$\left(\frac{1}{c} \frac{\partial}{\partial t} + \frac{1}{R} \right) v_1 = \frac{1}{4R^2} \left[\left(1 - \frac{1}{2} \right)^2 + \frac{\partial^2}{\partial \theta^2} \right] 2\phi + v_2,$$

$$\left(\frac{1}{c} \frac{\partial}{\partial t} + \frac{2}{R} \right) v_2 = \frac{1}{4R^2} \left[\left(2 - \frac{1}{2} \right)^2 + \frac{\partial^2}{\partial \theta^2} \right] v_1 + v_3,$$

$$\vdots \tag{102}$$

$$\left(\frac{1}{c} \frac{\partial}{\partial t} + \frac{j}{R} \right) v_j = \frac{1}{4R^2} \left[\left(j - \frac{1}{2} \right)^2 + \frac{\partial^2}{\partial \theta^2} \right] v_{j-1} + v_{j+1},$$

$$\vdots \tag{103}$$

$$\left(\frac{1}{c} \frac{\partial}{\partial t} + \frac{p}{R} \right) v_p = \frac{1}{4R^2} \left[\left(p - \frac{1}{2} \right)^2 + \frac{\partial^2}{\partial \theta^2} \right] v_{p-1}. \tag{104}$$

Let $\boldsymbol{v}(\theta,t) = \{v_j(\theta,t)\}$, $j = 1, 2, \ldots, p$, be defined as a time-dependent vector of order p, i.e., $\boldsymbol{v} = [v_1, v_2, \ldots, v_p]^{\mathrm{T}}$. Then the sequence (104) may be formulated as a coupled system of first-order partial differential equations in matrix form

$$\frac{1}{c}\frac{\partial \boldsymbol{v}}{\partial t} + \boldsymbol{A}_1 \boldsymbol{v} = \boldsymbol{A}_2 \frac{\partial^2 \boldsymbol{v}}{\partial \theta^2} + \boldsymbol{b}\phi(R,\theta,t), \quad \theta \in [0, 2\pi), \ t \geqslant 0 \tag{105}$$

with periodic and initial conditions, $\boldsymbol{v}(0,t) = \boldsymbol{v}(2\pi,t)$, $\boldsymbol{v}(\theta,0) = 0$. In the above $\boldsymbol{A}_1$ and $\boldsymbol{A}_2$ are constant $p \times p$, tri-diagonal and uni-diagonal matrices, respectively, defined with band

$$\boldsymbol{A}_1 = \frac{-1}{R}B\left[\frac{1}{4R}\left(j - \frac{1}{2}\right)^2, -j, R\right], \quad \boldsymbol{A}_2 = \frac{1}{4R^2}B[1,0,0]. \tag{106}$$

Similarly, the constant vector $\boldsymbol{b} = \{b_j\}$ is split as

$$\boldsymbol{b} = \boldsymbol{b}_1 + \boldsymbol{b}_2\frac{\partial^2}{\partial \theta^2}, \tag{107}$$

$$\boldsymbol{b}_1 = \frac{1}{8R^2}[1,0,\ldots,0]^{\mathrm{T}}, \quad \boldsymbol{b}_2 = \frac{1}{2R^2}[1,0,\ldots,0]^{\mathrm{T}}.$$

A variational equation for the boundary equations is obtained by multiplying (105) with a weighting function $\bar{v}$, and integrating-by-parts over the circular boundary Γ. Similarly, multiplying the wave equation (1) by the weighting function $\bar{\phi}$, integrating over the interior domain Ω, using the divergence theorem, and incorporating the local radiation condition (101) evaluated on the circular boundary at $r = R$ leads to the variational equation within the computational domain $\Omega \cup \partial\Omega$. Then, under the usual regularity conditions, the statement of the weak form for the coupled variational equations may be stated as:

Given load data and initial conditions,

Find $\phi(\boldsymbol{x},t)$, $\boldsymbol{x} \in \Omega \cup \partial\Omega$, and $\boldsymbol{v}(\theta,t)$, $\theta \in [0,2\pi]$, for $t \geqslant 0$, such that for all admissible functions $\bar{\phi}$ and $\bar{v}$:

$$M_\phi\left(\bar{\phi},\frac{\partial^2\phi}{\partial t^2}\right) + c_\phi\left(\bar{\phi},\frac{\partial\phi}{\partial t}\right) + K_\phi(\bar{\phi},\phi) = F_S(\bar{\phi}) + \int_\Gamma \bar{\phi}v_1 \,\mathrm{d}\Gamma, \tag{108}$$

$$C_v\left(\bar{\boldsymbol{v}},\frac{\partial\boldsymbol{v}}{\partial t}\right) + K_v(\bar{\boldsymbol{v}},\boldsymbol{v}) = \int_\Gamma \bar{\boldsymbol{v}}\cdot\boldsymbol{b}_1\phi \,\mathrm{d}\Gamma - \int_\Gamma \frac{\partial\bar{\boldsymbol{v}}}{\partial\theta}\cdot\boldsymbol{b}_2\frac{\partial\phi}{\partial\theta} \,\mathrm{d}\Gamma, \tag{109}$$

with

$$C_v(\bar{\boldsymbol{v}},\boldsymbol{v})_\Gamma := \frac{1}{c}\int_\Gamma \bar{\boldsymbol{v}}\cdot\boldsymbol{v} \,\mathrm{d}\Gamma,$$

$$K_v(\bar{\boldsymbol{v}},\boldsymbol{v}) := \int_\Gamma \bar{\boldsymbol{v}}\cdot\boldsymbol{A}_1\boldsymbol{v} \,\mathrm{d}\Gamma + \int_\Gamma \frac{\partial\bar{\boldsymbol{v}}}{\partial\theta}\cdot\boldsymbol{A}_2\frac{\partial\boldsymbol{v}}{\partial\theta} \,\mathrm{d}\Gamma,$$

and M_ϕ, C_ϕ, K_ϕ were defined earlier in (45)–(47), respectively. The function $v_1(\theta,t)$ is the first element of the vector array $\boldsymbol{v}(\theta,t) = \{v_j(\theta,t)\}$, which satisfies (109) driven by $\phi(R,\theta,t)$.

We next apply the standard Galerkin semi-discrete approximations

$$\phi(\boldsymbol{x},t) \approx \phi^h(\boldsymbol{x},t) = \boldsymbol{N}(\boldsymbol{x})\boldsymbol{d}_\phi(t), \tag{110}$$

$$\boldsymbol{v}(\theta,t) \approx \boldsymbol{v}^h(\theta,t) = \boldsymbol{N}_v(\theta)\boldsymbol{d}_v(t). \tag{111}$$

Here, $\boldsymbol{N}(\boldsymbol{x})$ is a row vector of standard C^0 basis functions with compact support associated with each node in the interior and the boundary, and $\boldsymbol{d}_\phi(t)$ is a time-continuous column vector containing the nodal values of ϕ^h. Similarly, $\boldsymbol{N}_v(\theta)$ is a matrix of basis functions associated with the global solution vector

$d_v(t)$ defined on the boundary Γ. Here $d_v(t)$ is a vector dimension $p \times N_\Gamma$, and defined by $d_v(t) = \{v_A(t)\}$, with nodal values $v_A(t) = v^h(\theta_A, t)$, $A = 1, 2, \ldots, N_\Gamma$. We denote N_Γ as the total number of nodes on the boundary Γ, and p as the number of auxiliary functions included in the sequence of local boundary operators.

Using this approximation in (108) and (109), we arrive at the following coupled semi-discrete equations:

$$M_\phi \ddot{d}_\phi(t) + C_\phi \dot{d}_\phi(t) + K_\phi d_\phi(t) = f_S(t) + \int_\Gamma N_\phi^{\mathrm{T}} v_1^h(\theta, t)\, \mathrm{d}\Gamma, \tag{112}$$

$$C_v \dot{d}_v(t) + K_v d_v(t) = \int_\Gamma N_v^{\mathrm{T}} b_1 \phi^h\, \mathrm{d}\Gamma - \int_\Gamma N_{v,\theta}^{\mathrm{T}} b_2 \phi_{,\theta}^h\, \mathrm{d}\Gamma. \tag{113}$$

In the above, M_ϕ, C_ϕ, and K_ϕ are standard symmetric, sparse arrays associated with the finite element discretization of the wave equation and the local B_1 operator. The function $v_1^h(\theta, t) = \sum_{A=1}^{N_\Gamma} N_A(\theta) v_1^A(t)$ is the first element of the vector array $v^h = \{v_j^h\}$. The sparse matrices C_v and K_v follow from the form of the variational equation (109). We note that C_v is symmetric, while K_v is non-symmetric. In two-dimensions, these matrices may be computed in closed-form. For example, with linear Lagrange interpolation with Gauss–Lobatto (nodal) quadrature, the matrices can be expressed in nodal block tridiagonal form, with band:

$$C_v = \frac{1}{c} B[\mathbf{0}, \delta\theta_A I_p, \mathbf{0}], \tag{114}$$

$$K_v = B\left[\frac{-2}{\Delta\theta_{A-1}} A_2, \left(\delta\theta_A A_1 + \frac{2\delta\theta_A}{\Delta\theta_A \Delta\theta_{A-1}} A_2 \right), \frac{-2}{\Delta\theta_{A-1}} A_2 \right], \tag{115}$$

where $\Delta\theta_A = \theta_{A+1} - \theta_A$, and $\delta\theta_A = \theta_{A+1} - \theta_{A-1}$, $A = 1, 2, \ldots, N_\Gamma$, and I_p is the identity matrix with dimension $p \times p$. For a full circular boundary the matrix K_v has an additional block $A_2/\Delta\theta_{N_\Gamma}$ in the corners due to the periodic conditions.

Similarly, the nodal partition for the coupling vector on the right-hand side of (113) may be written in closed form as

$$\{f_v\}_A = \delta\theta_A \phi_A b_1 + 2\left(\frac{\Delta\phi_A}{\Delta\theta_A} - \frac{\Delta\phi_{A-1}}{\Delta\theta_{A-1}} \right) b_2, \tag{116}$$

where $\phi_A = (d_v)_A$, $A = 1, 2 \ldots, N_\Gamma$ is a nodal value on the boundary Γ, and $\Delta\phi_A = \phi_{A+1} - \phi_A$.

Since the boundary matrix K_v has a non-symmetric component, we avoid solving the coupled interior/boundary equations with a single time-integrator algorithm. Instead we use a mixed integration approach which allows for a natural and independent integration of the interior and boundary equations, with coupling through the boundary force vectors at each time step. Several different time-marching schemes are developed to integrate the symmetric second-order equations (112) concurrently with the non-symmetric first-order equations (113).

In the first method, we apply the Newmark family of algorithms (or variations such as HHT-α) to integrate (112). Let $d^k = d_\phi(t_k)$, $u^k = \dot{d}_\phi(t_k)$, $a^k = \ddot{d}_\phi(t_k)$, be the numerical solution and $f^k = f(t_k)$ the RHS vector at time step $t_k = k\Delta t$, the the Newmark method in predictor/corrector form may be expressed as [38]:

First predict,

$$\tilde{d}^{k+1} = d^k + \Delta t u^k + \frac{\Delta t^2}{2}(1 - 2\beta)a^k,$$

$$\tilde{u}^{k+1} = u^k + (1 - \gamma)\Delta t a^k.$$

Solve a^{k+1}:

$$(M_\phi + \gamma\Delta t C_\phi + \beta\Delta t^2 K_\phi)a^{k+1} = f_\phi^{k+1} - C_\phi \tilde{u}^{k+1} - K_\phi \tilde{d}^{k+1}. \tag{117}$$

Then correct,

$$\boldsymbol{d}^{k+1} = \tilde{\boldsymbol{d}}^{k+1} + \beta\Delta t^2 \boldsymbol{a}^{k+1},$$

$$\boldsymbol{u}^{k+1} = \tilde{\boldsymbol{u}}^{k+1} + \gamma\Delta t \boldsymbol{a}^{k+1}.$$

Here we use the *implicit* second-order accurate $\gamma = 1/2$, and unconditionally stable trapezoidal rule ($\beta = 1/4$). Use of unconditionally stable methods allows for automation of adaptive grids and time stepping algorithms. Using the solution from the previous time step for an initial guess efficient iterative solutions of (117) are possible with only a few iterations due to the local character of time-dependent wave solutions. Since the matrices are symmetric and positive-definite, the well-understood preconditioned Conjugate Gradient iterative solver is appropriate. The solution of (117) requires that the forcing term $\boldsymbol{f}_\phi^{k+1} = \boldsymbol{f}_S^{k+1} + \boldsymbol{f}_\Gamma^{k+1}$ be available at time step t_{k+1}, i.e.,

$$\boldsymbol{f}_\Gamma^{k+1} = R \int_0^{2\pi} \boldsymbol{N}^{\mathrm{T}} v_1^h(\theta, t_{k+1}) \, \mathrm{d}\theta. \tag{118}$$

To reduce cost, this integral may be evaluated using nodal quadrature, with the result

$$(\boldsymbol{f}_\Gamma)_A^{k+1} = (v_1)_A^{k+1} R M_A, \quad \theta_A \in \Gamma,$$

where $(v_1)_A^{k+1} = v_1^h(\theta_A, t_{k+1})$, and $M_A = \mathrm{diag}(\boldsymbol{M}_\Gamma)$.

Let $\boldsymbol{d}_v^{k+1} = \boldsymbol{d}_v(t_{k+1})$, then $(v_1)_A^{k+1}$, may be updated using the second-order accurate Adams–Bashforth *explicit* algorithm [39]:

$$\boldsymbol{d}_v^{k+1} = \boldsymbol{d}_v^k + \frac{\Delta t}{2} \boldsymbol{C}_v^{-1} \left[3(\boldsymbol{f}_v^k - \boldsymbol{K}_v \boldsymbol{d}_v^k) - (\boldsymbol{f}_v^{k-1} - \boldsymbol{K}_v \boldsymbol{d}_v^{k-1}) \right]. \tag{119}$$

Using linear interpolation with Gauss–Lobatto quadrature, and the closed-form nodal block matrix form given in (115) and (116), the solution to (119) for the values $(v_j)_A^{k+1} = v_j^h(\theta_A, t_{k+1})$, at node A, may be computed in sequence for $j = 1, 2, \ldots, p$ and $A = 1, 2, \ldots, N_\Gamma$ from the difference equation:

$$(v_j)_A^{k+1} = (v_j)_A^k - j\gamma[3(v_{j-1})_A^k - (v_j)_A^{k-1}] + \gamma R[3(v_{j+1})_A^k - (v_{j+1})_A^{k-1}]$$
$$+ \frac{\gamma}{4R}\left[\left(j - \frac{1}{2}\right)^2 + \delta^2\right][3(v_{j-1})_A^k - (v_{j-1})_A^{k-1}],$$

with $(v_0)_A = 2\phi_A$ and $(v_{p+1})_A = 0$. In the above $(v_j)_A^k$ denotes the jth auxiliary function at node A and time-step k, $\gamma = c\Delta t/2R$, and δ^2 is defined by the second-order spatial difference operator on a non-uniform grid

$$\delta^2(v_j)_A = \frac{1}{\alpha_A^2}[\beta_A(v_j)_{A-1} - (1 + \beta_A)(v_j)_A + (v_j)_{A+1}],$$

$$\frac{1}{\alpha_A^2} := \frac{2}{\beta_A(1 + \beta_A)\Delta\theta_{A-1}^2}, \quad \beta_A = \Delta\theta_A/\Delta\theta_{A-1}.$$

Alternatively, the solution $\boldsymbol{d}_\phi(t)$ may be advanced using a second-order accurate *explicit* time-integration method:

$$\boldsymbol{d}_\phi^{k+1} = \left[\frac{1}{\Delta t^2}\boldsymbol{M}_\phi + \frac{1}{2\Delta t}\boldsymbol{C}_\phi\right]^{-1} \boldsymbol{R}^k,$$

$$\boldsymbol{R}^k = \boldsymbol{f}_\phi^k - \left[\boldsymbol{K}_\phi - \frac{1}{\Delta t^2}\boldsymbol{M}_\phi\right]\boldsymbol{d}_\phi^k - \left[\frac{1}{\Delta t^2}\boldsymbol{M}_\phi - \frac{1}{2\Delta t}\boldsymbol{C}_\phi\right]\boldsymbol{d}_\phi^{k-1}. \tag{120}$$

With Gauss–Lobatto quadrature the matrices $\boldsymbol{M}_\phi$ and $\boldsymbol{C}_\phi$ are diagonal, and the above equations may be solved independently, without matrix factorization. Then the auxiliary functions may be updated using an *implicit* method such as the second-order accurate Adams–Moulton method:

$$\left(\boldsymbol{C}_v + \frac{\Delta t}{2}\boldsymbol{K}_v\right)\boldsymbol{d}_v^{k+1} = \left(\boldsymbol{C}_v - \frac{\Delta t}{2}\boldsymbol{K}_v\right)\boldsymbol{d}_v^k + \frac{\Delta t}{2}\left(\boldsymbol{f}_v^{k+1} + \boldsymbol{f}_v^k\right). \tag{121}$$

Instead, we may use a *semi-explicit* method to solve the auxiliary equations as suggested by Hagstrom and Hariharan [28]. To this end, we split the sparse matrix $\boldsymbol{K}_v = \boldsymbol{L} + \boldsymbol{U}$ into a lower part including diagonal $\boldsymbol{L}$, and a strictly upper part $\boldsymbol{U}$. The upper part is treated explicitly using the second-order accurate Adams–Bashforth method, while the remaining lower part is integrated with the implicit trapezoidal rule. With this method, we advance the solution using the algorithm:

$$\hat{\boldsymbol{L}}\boldsymbol{d}_v^{k+1} = \left[\boldsymbol{C}_v - \frac{\Delta t}{2}(\boldsymbol{L} + 3\boldsymbol{U})\right]\boldsymbol{d}_v^k + \frac{\Delta t}{2}\boldsymbol{U}\boldsymbol{d}_v^{k-1} + \frac{\Delta T}{2}\left(\boldsymbol{f}_v^{k+1} + \boldsymbol{f}_v^k\right), \tag{122}$$

where $\boldsymbol{d}_v^{k+1}$ is solved in sequence for $j = 1, 2\ldots, p$ and $A = 1, 2, \ldots, N_\Gamma$ using a forward sweep of the lower triangle matrix

$$\hat{\boldsymbol{L}} = \boldsymbol{C}_v + \frac{\Delta t}{2}\boldsymbol{L}.$$

With linear interpolation and Gauss–Lobatto quadrature the solution $(v_j)_A^{k+1}$ to (122) for the jth auxiliary function at node A, and time-step $k+1$, may be computed in sequence for $j = 1, 2, \ldots, p$ and $A = 1, 2, \ldots, N_\Gamma$ from the difference equation:

$$[1 + j\gamma](v_j)_A^{k+1} = [1 - j\gamma](v_j)_A^k + \gamma R[3(v_{j+1})_A^k - (v_{j+1})_A^{k-1}] + \frac{\gamma}{4R}\left[\left(j - \frac{1}{2}\right)^2 + \delta^2\right][(v_{j-1})_A^{k+1} + (v_{j-1})_A^k]$$

with $(v_0)_A^k = 2\phi_A^k$ and $(v_{p+1})_A^k = 0$.

   With $p = P$ auxiliary functions and N_Γ node points on the circular radiation boundary, direct implementation of the recursive sequence of local operators requires work and storage of order $O(N_\Gamma P)$. This compares to the work and storage for the auxiliary functions of order $O(N_T P)$ together with storage $O(N_\Gamma)$ and work $O(N_\Gamma N_T)$ required to compute the inner products in the Fourier transforms in the modal form discussed in Section 4 (or $O(N_\Gamma \log N_\Gamma)$ work using FFT with $N_T = N_\Gamma$). For a typical problem, $P \leqslant N_T \leqslant N_\Gamma$, so that the work required using the direct implementation is slightly less than that required for the modal form, while the storage is slightly higher than for the modal form. In both the direct and modal implementations, the amount of work is less than that required for calculation of the interior domain.

   To compare the accuracy and stability properties of the direct implementation of the asymptotic RBCs vs. the tangential Fourier mode expansion implementation, we revisit the problem of radiation from a line element in a circular baffle discussed earlier in Section 6.1. We consider the following time-integration algorithms for the finite element semi-discrete equations for the interior domain, together with the radiation boundary discretization:

Direct implementation:

Algorithm	Interior	Boundary
C1(P)	Implicit using (117)	Explicit using (119)
C2(P)	Explicit using (120)	Implicit using (121)
C3(P)	Explicit using (120)	Semi-explicit using (122)

Tangential Fourier expansion implementation described earlier in Section 4:

Algorithm	Interior	Boundary
A1(N,P)	Implicit using (65) in [22]	Explicit using (69) in [22]
A2(N,P)	Explicit using (61) in [22]	Implicit using (73) in [22]

In the above, we denote by $C^*(P)$, time-integration algorithms based on the implementation of the sequence of local RBCs, with P denoting the number of auxiliary functions included. For comparison we denote by $A^*(N,P)$ algorithms based on the tangential implementations of RBC1(N,P), using N terms in the Fourier mode expansion.
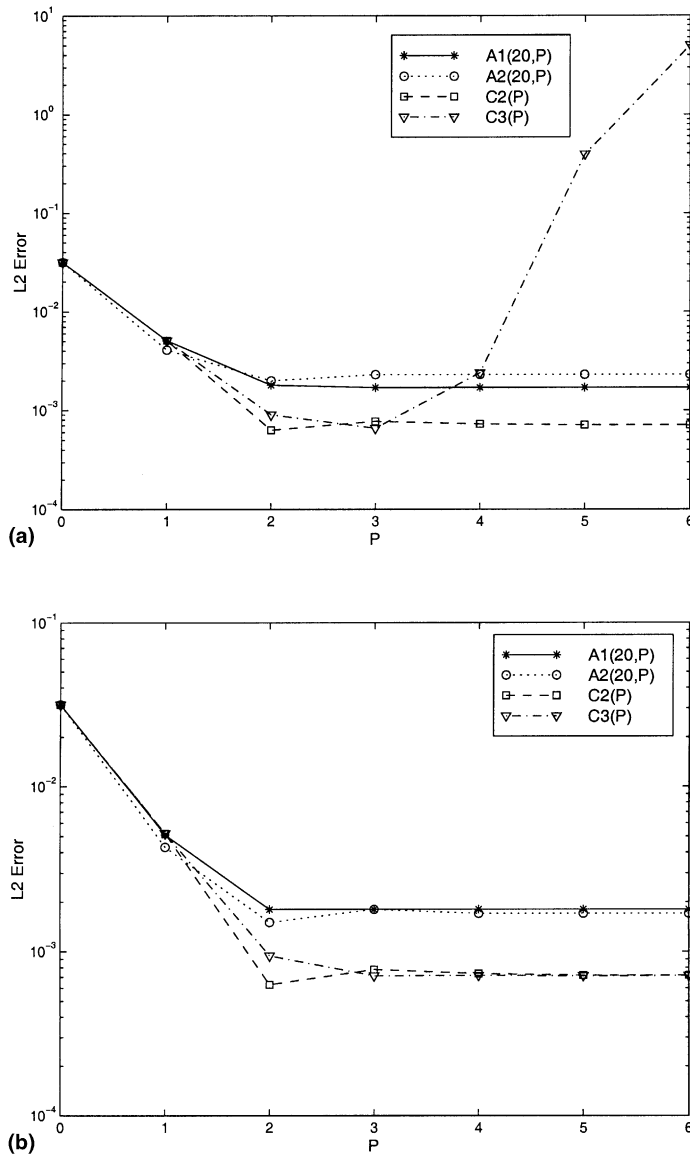
Fig. 17. Maximum L_2 error during steady state for problem of radiation from a line element on a circular cylinder. 'Course mesh' (15×120). (a) $\Delta t = 0.01$, (b) $\Delta t = 0.0075$.

Figs. 17 and 18 show the maximum L_2 error during steady-state measured at $R/a = 1.75$, and variable P. Results are compared for a 'course mesh' of (15×120) and a 'fine mesh' of (30×240) elements in the radial and circumferential directions, respectively. Results show that for each of the algorithms tested, as the order P is increased, the error is rapidly reduced to the discretization level. We note that algorithms A1 and C1 give nearly identical results and therefore only A1 is shown in the graphs. For the course mesh, algorithms C2 and C3, which are based on the explicit time integration of the interior equations, together with implicit and semi-implicit integration of the local boundary operators display a lower discretization error compared to A1 and A2. For the fine mesh, the level of relative discretization error between the different algorithms is mixed, probably a result of the precise solutions obtained and numerical variations in the interplay between the mesh size and time step used.

An important observation from these results is that algorithms C2 and C3 may become unstable as the number of auxiliary functions P is increased beyond that which is required to reduce the error to the
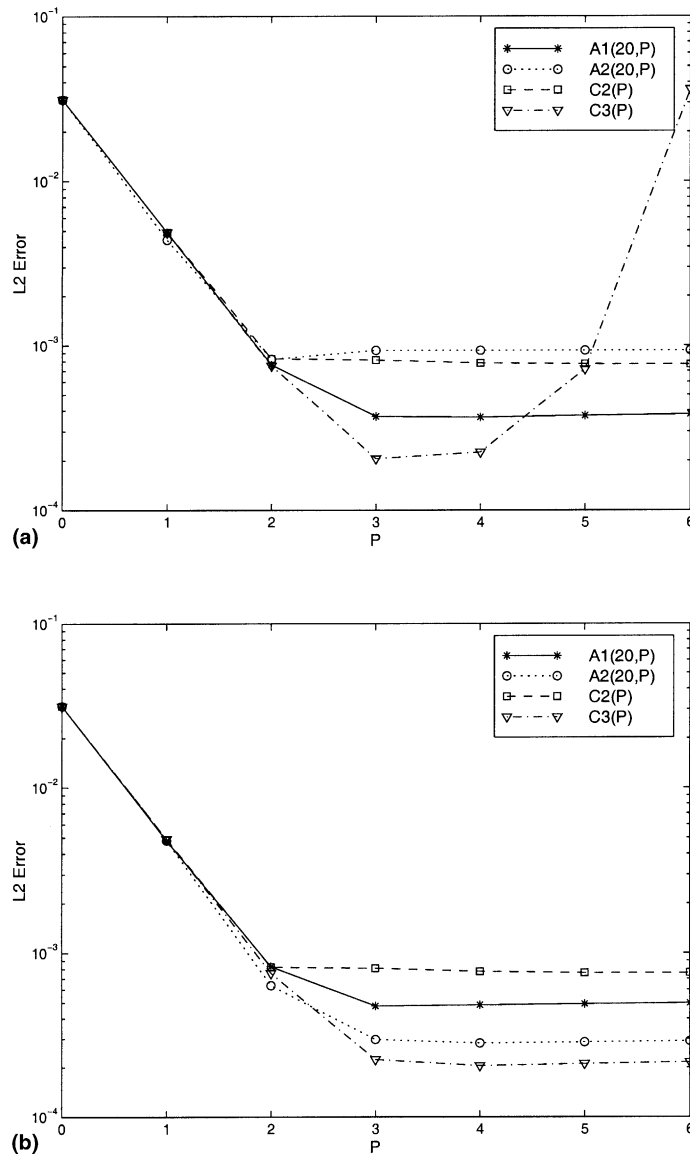

Fig. 18. Maximum L_2 error during steady state for problem of radiation from a line element on a circular cylinder. 'Fine mesh' (30×240). (a) $\Delta t = 0.004$, (b) $\Delta t = 0.001$.
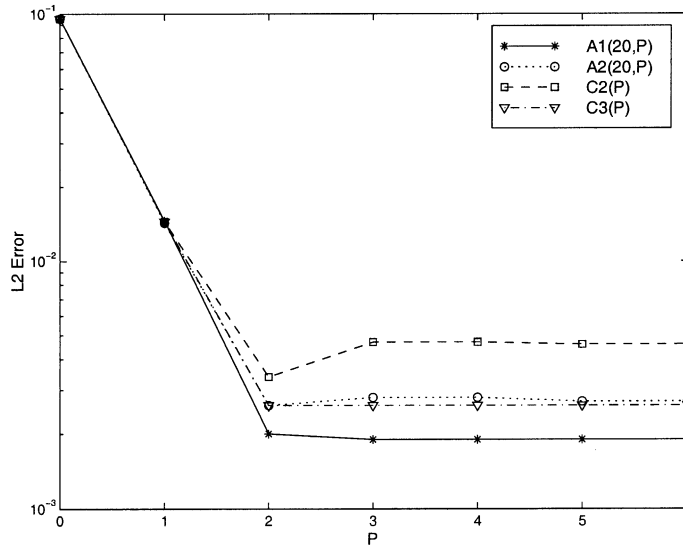
Fig. 19. Maximum L_2 error during steady state for the problem of scattering from a circular cylinder. Mesh (30×240), time-step $\Delta t = 0.001$, radiation boundary $R/a = 1.75$, frequency $\omega a/c = \pi$.
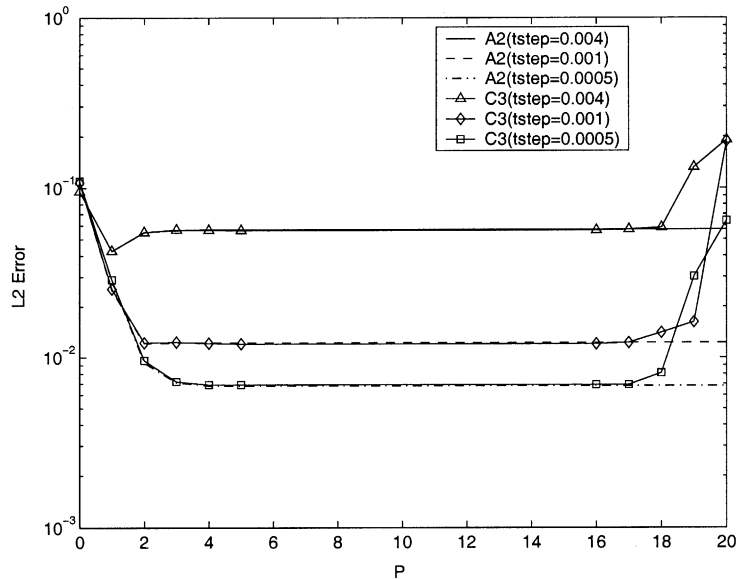

Fig. 20. Maximum L_2 error during steady state for elliptic scattering problem. Comparisons of algorithms A2(P) and C3($20, P$) with different time step size.

discretization level. For the course mesh and time step $\Delta t = 1.0 \times 10^{-2}$, algorithms C2 and C3 become unstable starting at $P = 14$ and $P = 4$, respectively. As the time step is decreased to $\Delta t = 0.75 \times 10^{-2}$, algorithm C2 becomes unstable starting at $P = 13$, while C3 remains stable for all values of P tested ($P \leqslant 30$). For the fine mesh solution with $\Delta t = 0.4 \times 10^{-2}$, algorithms C2 and C3 become unstable starting at $P = 12$ and $P = 5$, respectively; with $\Delta t = 0.10 \times 10^{-2}$, then algorithms C2 and C3 become unstable starting at $P = 10$ and $P = 25$, respectively. We should point out that for this problem, only $P = 3$ auxiliary functions are need to reach the discretization error – well below the stability limits exhibited by C2, for both meshes and time steps tested. The stability of C3 is more sensitive to the time step used – instability occurs at relatively small values for the larger time step for both meshes, yet remains relatively stable when using small time steps. Algorithms A1, A2 and C1 remained stable for all mesh sizes and time steps tested.

Similar observations are found when solving the scattering problems from circular and elliptic cylinders, as described earlier in Sections 6.2 and 6.3. Figs. 19 and 20 show the maximum L_2 error during steady-state measured on the radiation boundary for these problems. For the circular cylinder using mesh (30×240), and $\Delta t = 0.001$. Algorithms C2 and C3 become unstable starting at very large orders $P = 22$ and $P = 28$, respectively. Similarly for the elliptic scatterer, for very high-orders $P > 16$, well after the solution has reached the level of the discretization error, algorithm C3 becomes unstable. These results show that the semi-explicit scheme for the auxiliary functions, while extremely efficient, is only conditionally stable and is sensitive to space-time discretization and order P. Fortunately, due to the rapid reduction of the residual functions in the boundary conditions, only a relatively low-order value P is required, resulting in stable solutions. Additional numerical results on unstructured meshes are given in [2]. On the whole, algorithms A1 and C1 were the most robust, showing good accuracy with stable solutions for all the test problems studied to date.

8. Conclusions

The recursive sequence of local RBCs first given by Hagstrom and Hariharan [28] for the numerical solution of the time-dependent wave equation in a exterior region are considered. In this paper we have rederived this sequence from direct application of the hierarchy of local boundary operators of Bayliss and Turkel [13] and a recursion relation for the expansion coefficients appearing in the 2D asymptotic wave expansion. A modified version similar to the formulation given in [25,27] was also reported. These boundary conditions are local and involve auxiliary variables to remove the high order derivatives in r and t, present in the original boundary operators of Bayliss and Turkel. With this reformulation, the auxiliary functions are recognized as residuals of the local boundary operators acting on the asymptotic wave expansion. By introducing a decomposition of the auxiliary variables into tangential Fourier modes we reformulate the sequence of local boundary conditions in integro-differential form involving systems of first-order temporal equations for the auxiliary functions associated with each mode and the tangential Fourier transform of the solution evaluated on the boundary. A similar decomposition was used in [27] for the three-dimensional wave equation on a sphere. Computation of eigenvalues verified solutions to the first-order system of residual functions for each mode are stable. To compute the far-field solution we use a second-order explicit finite difference equation separately for each Fourier mode. The reformulation of the auxiliary functions in terms of a tangential Fourier mode expansion easily fits into standard finite element discretization for the interior domain without altering the symmetric and sparse character of the finite element equations.

We showed that inner-products required by the Fourier transform of the solution evaluated on the boundary and inverse Fourier transform of the auxiliary function can be computed efficiently using trig function recursion or Fast Fourier Transforms (FFTs). When the total number of modes $N_T = 2N + 1$ included in the tangential Fourier mode expansion is less than the number of node points on the boundary N_Γ, (a factor of five or more is typical), then a trig function recursion algorithm may be used with $O(N_\Gamma N_\Gamma)$ operations and storage requirements of $O(N_\Gamma)$ words. When the number of modes in the series expansion is increased to the number of points on the boundary, then the FFT may be used to compute the inner products, with number of operations $O(N_\Gamma \log N_\Gamma)$. In both cases, the work and storage is less than the $O(N_\Gamma^2)$ work required for the finite element calculation in the interior domain. The work per time step and storage associated with calculation of the auxiliary functions is proportional to $N_P = O(N_T P)$, where P is the maximum number of residual functions included, independent of the number of points used on the boundary. Typically, $P \ll N_T$, and the work and storage is negligible compared to the work and storage required to calculate the interior finite element equations and Fourier transforms.

The finite element implementations with efficient calculation of Fourier transforms described here may be used to formulate other similar RBCs, for example of the rational approximations to the non-reflecting boundary kernel as a sum of poles as given in [31]. In that case, the auxiliary function $v_{n,1}(t)$ appearing our radiation condition would be replaced by a summation over other auxiliary functions satisfying a similar first-order system of differential equations with the real-valued coefficients replaced with complex pole coefficients.

Comparisons of our tangential Fourier mode expansion with direct finite element implementations of the sequence of local boundary conditions were given. To avoid destroying the symmetric structure of the interior matrix equations, we presented several mixed time integration algorithms which allow for a natural and independent integration of the interior and boundary equations, with coupling through the boundary force vectors at each time step. Direct implementation of the recursive sequence of local operators requires work and storage of order $O(N_\Gamma P)$. Typically, $P \leqslant N_T \leqslant N_\Gamma$, so that the work required using the direct implementation is slightly less than that required for the modal form with order $O(N_\Gamma N_T)$, while the storage is slightly higher than for the modal form with $O(N_\Gamma)$. In both the direct and modal implementations, the amount of work is less than that required for calculation of the interior domain. One advantage of the tangential modal implementation is that far-field solutions may be computed *concurrently* with the near-field solution without saving time-history data at interior points, as described in [24].

Numerical studies show that our direct and tangential Fourier mode expansion implementations exhibit similar discretization errors. However, for the direct implementation, when using explicit time integration for the interior domain combined with implicit or semi-explicit time integrators for the auxiliary equations, the solutions may become unstable when a large number of auxiliary functions are included beyond that required to obtain accurate solutions. Implicit time integration for the interior domain combined with explicit time integration for the boundary equations, both for the direct and tangential Fourier mode implementations, provided the most robust algorithms, giving good accuracy with stable solutions for all the test problems studied to date.

In the two-dimensional case considered here, the RBCs are based on an asymptotic wave expansion which does not converge at any fixed radius. However, for many practical problems truncating the asymptotic expansion after P terms provides solutions with errors well below that of the discretization error. As the number of residual functions included in the sequence of RBCs increases, the error in the asymptotic condition is rapidly driven down to the space-time discretization error. Numerical results show that even for very low frequencies the sequence of high-order conditions progressively reduces the error compared to low-order approximations. Accurate solutions for low frequencies may be obtained to any practical order desired by increasing the number of residual functions combined with an expansion of the domain (boundary extension). The use of boundary extension would, however, increase the size of the computational domain, and in this low-frequency limit, other approximate conditions would be appropriate, such as the DAA or the convergent rational approximates in [31]. Error estimates for the Hagstrom and Hariharan local operators given in [4] indicate that the boundary extension required may be modest. However, further research is needed to obtain rigorous a priori estimates in integral norms for the accuracy of the asymptotic RBCs, both as a function of the number of angular modes N, the number of residual functions used P, the radial distance R, and the time span of the analysis.

Acknowledgements

References

[1] L.L. Thompson, R. Huan, Asymptotic and exact radiation boundary conditions for time-dependent scattering, in: Proceedings of the ASME Noise Control and Acoustics Division – 1999, ASME 1999 International Mechanical Engineering Congress and Exposition, Nashville, TN, November 14–19 (Symposium on Computational Acoustics), NCA-vol. 26, 1999, pp. 511–521.

[2] L.L. Thompson, D. He, R. Huan, Implementation of local, high-order accurate boundary conditions for time-dependent acoustic scattering, in: Proceedings of the ASME Noise Control and Acoustics Division – 2000, The 2000 ASME International Mechanical Engineering Congress and Exposition, Orlando, FL, November 5–10, 2000 (Session: Computational Acoustics), NCA-vol. 27, The American Society of Mechanical Engineers, 2000, pp. 27–38.

[3] S. Tsynkov, Numerical solution of problems on unbounded domains. A review, Appl. Numer. Math. 27 (1998) 465–532.

[4] T. Hagstrom, Radiation boundary conditions for the numerical simulation of waves, Acta Numerica 8 (1999).

[5] P.M. Pinsky, L.L. Thompson, N.N. Abboud, Local high-order radiation boundary conditions for the two-dimensional time-dependent structural acoustics problem, J. Acoust. Soc. Am. 91 (3) (1992) 1320–1335.

[6] L.L. Thompson, P.M. Pinsky, A space-time finite element method for structural acoustics in infinite domains, part I: formulation, stability, and convergence, Comput. Methods Appl. Mech. Engrg. 132 (1996) 195–227.

[7] L.L. Thompson, P.M. Pinsky, A space-time finite element method for the exterior structural acoustics problem: time-dependent radiation boundary conditions in two spatial dimensions, Int. J. Numer. Methods Eng. 39 (1996) 1635–1657.

[8] L.W. Pearson, R.A. Whitaker, L.J. Bahrmasel, An exact radiation boundary condition for the finite-element solution of eletromagnetic scattering on an open domain, IEEE Trans. Magn. 25 (4) (1989) 3046–3048.

[9] J.B. Keller, D. Givoli, Exact non-reflecting boundary conditions, J. Comput. Phys. 82 (1989) 172–192.

[10] M.J. Grote, J.B. Keller, On nonreflecting boundary conditions, J. Comput. Phys. 122 (1995) 231–243.

[11] L.L. Thompson, C. Ianculescu, R. Huan, Exact radiation conditions on spheroidal boundaries with sparse iterative methods for efficient computation of exterior acoustics, in: Proceedings of the 7th International Congress on Sound and Vibration (Session on Finite Elements in Acoustics), Garmisch–Partenkirchen, Germany, July 4–7, 2000, pp. 2101–2108.

[12] R.J. Astley, Infinite elements for wave problems: a review of current formulations and an assessment of accuracy, Int. J. Numer. Methods Engrg. 49 (2000) 951–976.

[13] A. Bayliss, E. Turkel, Radiation boundary conditions for wave-like equations, Commun. Pure Appl. Math. 33 (1980) 707–725.

[14] Q.H. Liu, J. Tao, The perfectly matched layer (PML) for acoustic waves in absorptive media, J. Acoust. Soc. Am. 102 (1997) 2072–2082.

[15] X. Yuan, D. Borup, J.W. Wiskin, M. Berggren, R. Eidens, S.A. Johnson, Formulation and validation of Berenger's PML absorbing boundary for the FDTD simulation of acoustic scatttering, IEEE Trans. Ultrason. Ferroelect. Freq. Contr. 44 (1997) 816–822.

[16] R.J. Astley, Transient wave-envelope elements for wave problems, J. Sound Vib. 192 (1996) 245–261.

[17] R.J. Astley, G.J. Macaulay, J.-P. Coyette, L. Cremers, Three-dimensional wave-envelope elements of variable order for acoustic radiation and scattering. Part II. Formulation in the time domain, J. Acoust. Soc. Am. 103 (1998) 64–72.

[18] R.J. Astley, Transient spheroidal elements for unbounded wave problems, Comput. Methods Appl. Mech. Engrg. 164 (1998) 3–15.

[19] J.L. Cipolla, M.J. Butler, Infinite elements in the time domain using a prolate spheroidal multipole expansion, Int. J. Numer. Methods Engrg. 43 (1998) 889–908.

[20] M.J. Grote, J.B. Keller, Exact non-reflecting boundary conditions for the time dependent wave equation, SIAM J. Appl. Math. 55 (1995) 280–297.

[21] M.J. Grote, J.B. Keller, Nonreflecting boundary conditions for time dependent scattering, J. Comput. Phys. 127 (1996) 52–65.

[22] L.L. Thompson, R. Huan, Implementation of exact non-reflecting boundary conditions in the finite element method for the time-dependent wave equation, Comput. Methods Appl. Mech. Engrg. 187 (2000) 137–159.

[23] H. Lamb, Hydrodynamics, fourth ed., Cambridge University Press, Cambridge, 1916, p. 517, Eq. (4).

[24] L.L. Thompson, R. Huan, Computation of far field solutions based on exact nonreflecting boundary conditions for the time-dependent wave equation, Comput. Methods Appl. Mech. Engrg. 190 (2000) 1551–1577.

[25] L.L. Thompson, R. Huan, Finite element formulation of exact non-reflecting boundary condition for the time-dependent wave equation, Int. J. Numer. Methods Engrg. 45 (1999) 1607–1630.

[26] L.L. Thompson, R. Huan, Computation of transient radiation in semi-infinite regions based on exact nonreflecting boundary conditions and mixed time integration, J. Acoust. Soc. Am. 106 (6) (1999) 3095–3108.

[27] R. Huan, L.L. Thompson, Accurate radiation boundary conditions for the time-dependent wave equation on unbounded domains, Int. J. Numer. Methods Engrg. 47 (2000) 1569–1603.

[28] T. Hagstrom, S. Hariharan, A formulation of asymptotic and exact boundary conditions using local operators, Appl. Numer. Math. 27 (1998) 403–416.

[29] T. Hagstrom, S.I. Hariharan, R.C. MacCamy, On the accurate long-time solution of the wave equation in exterior domains: asymptotic expansions and corrected boundary conditions, Math. Comput. 63 (1994) 507–539.

[30] T. Hagstrom, On high-order radiation boundary conditions, in: B. Engquist, G. Kriegsmann (Eds.), Computational Wave Propagation, IMA Vol. Math Appl., vol. 86, Springer, New York, 1996, pp. 23–43.

[31] B. Alpert, L. Greengard, T. Hagstrom, Rapid evaluation of nonreflecting boundary kernels for time-domain wave propagation, SIAM J. Numer. Anal. 37 (4) 1138–1164.

[32] B. Alpert, Time-domain algorithms for computational electromagnetics, http://www.boulder.nist.gov/itl/div891/alpert/td-em/index.html, July 2000.

[33] A. Barry, J. Bielak, R. MacCamy, On absorbing boundary conditions for wave propagation, J. Comput. Phys. 79 (1988) 449–468.

[34] D. Ludwig, Exact and asymptotic solutions of the Cauchy problem, Commun. Pure Appl. Math. 13 (1960) 473–508.

[35] L.F. Kallivokas, J. Bielak, R.C. MacCamy, Symmetric local absorbing boundaries in time and space, ASCE J. Engrg. Mech. 117 (1991) 2027–2048.

[36] A.A. Oberai, M. Malhotra, P.M. Pinsky, On the implementation of the Dirichlet-to-Neumann radiation condition for iterative solution of the Helmholtz equation, Appl. Numer. Math. 27 (1998) 443–464.

[37] A. Dutt, V. Rokhlin, Fast Fourier transform for nonequispaced data, SIAM J. Sci. Stat. Comput. (1993).

[38] T.J.R. Hughes, A precis of developments in computational methods for transient analysis, J. Appl. Mech. 50 (1983) 1033–1040.

[39] J. Butcher, The Numerical Analysis of Ordinary Differential Equations, Wiley, New York, 1987.

[40] T.L. Geers, Doubly asymptotic approximations for transient motions of submerged structures, J. Acoust. Soc. Am. 76 (1978) 1500–1508.
[41] C.A. Felippa, J.A. Deruntz, Finite element analysis of shock-induced hull cavitation, Comput. Methods Appl. Mech. Engrg. 44 (1984) 297–337.
[42] M. Abramowitz, I. Stegun (Eds.), Handbook of Mathematical Functions, National Bureau of Standards, Washington, DC, 1964. Reprinted by Dover Publications, New York, 1968.
[43] P.M. Morse, H. Feshbach, Methods of Theoretical Physics, McGraw-Hill, New York, 1953.